Internal Quantum Efficiency Measuring Setup

The probe is irradiated by monochromatic, chopped light. A light detector (D1) and its associated lock-in amplifier will monitor the incoming light intensity from a diverted light path. This detector is needed to monitor the incoming light intensity.
The main light path goes through a port inside an integrating sphere. A second detector, D2, (with its own lock-in amplifier) placed in a suitable port of the sphere will measure the intensity of incoming beam after multiple reflections inside the sphere. The readings of both detectors are correlated. From this moment further the detector D1 will give an accurate value for the incoming light inside the sphere.
The sample under test is placed diagonally opposed to the incoming beam. Its presence will affect the multiple reflections inside the sphere. The detector D2 will measure now the modified reflected light and another detector D3, the light transmitted through the sample (optional).
The absorbed light will be calculated then as the difference between the incoming intensity and the sum of reflected and transmitted intensities.
The same procedure is repeated automatically for all spectral wavelengths of interest.
The quantum efficiency is now calculated like the dependence of the collected charge carriers on the radiated photons of different wavelengths. In external spectral response the total number of photons is counted, whereas in the internal spectral response only those entering the probe are counted.
The collected charge carriers are measured through the short circuit current of the cell under variable light bias, as needed.

Please refer to the following diagram:

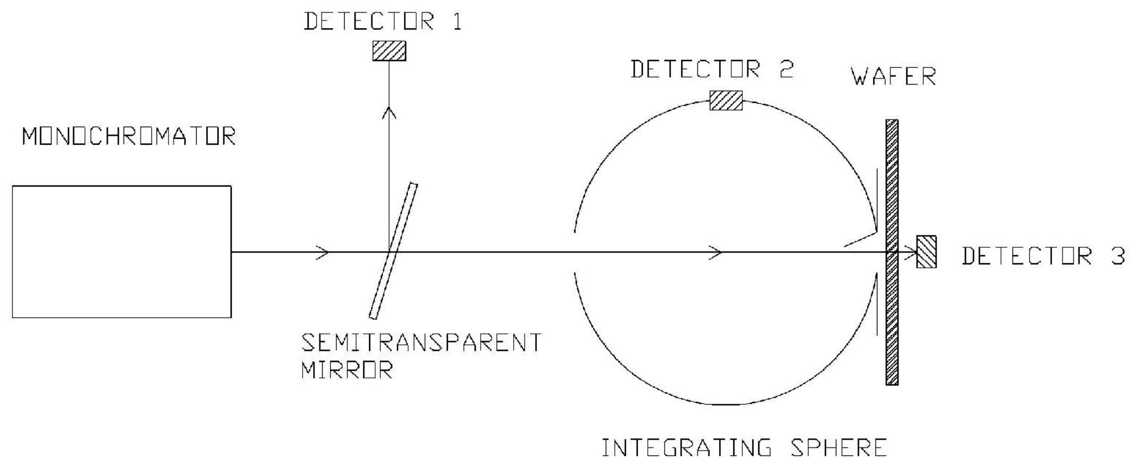

November 1998 NREL/CP-520-25654

UV-VIS-IR Spectral Responsivity Measurement System for Solar Cells

H. Field

Presented at the National Center for Photovoltaics Program Review Meeting, September 8–11, 1998, Denver, Colorado

National Renewable Energy Laboratory
1617 Cole Boulevard
Golden, Colorado 80401-3393
A national laboratory of
the U.S. Department of Energy
Managed by Midwest Research Institute
for the U.S. Department of Energy
under Contract No. DE-AC36-83CH10093

Prepared under Task No. PV903401

November 1998

UV-VIS-IR Spectral Responsivity Measurement System for Solar Cells

Halden Field

National Renewable Energy Laboratory (NREL)
1617 Cole Blvd., Golden, Colorado, USA 80401

Abstract. NREL's PV Cell and Module Performance Characterization group has built a new spectral responsivity measurement system for solar cells. It uses a xenon arc lamp source, a single, grating monochrometer, and a fiber-optic bundle to couple the monochromatic light to the test device. The system has a spectral bandwidth of 2 nm, minimum spot diameter of 1.6 mm, a spectral range of 280-1330 nm, and uncertainty better than ±3% over most of this range. It is capable of incorporating light bias with intensities exceeding one sun. This paper discusses the system's features, capabilities, calibration, and measurement uncertainties.

BACKGROUND

A photovoltaic (PV) device's spectral responsivity describes its ability to convert light of various wavelengths to electricity. It is often reported as the ratio of device current divided by incident-beam power (e.g., A/W) or device current divided by incident photon flux (i.e., quantum efficiency). Researchers can use spectral responsivity measurements to help understand device operation. Data from such measurements are also used in spectral mismatch parameter (1) calculations used to set solar simulator intensity for solar cell and module performance measurements.

SYSTEM DESCRIPTION

Figure 1 illustrates the system's major components and their configuration. Table 1 lists major system specifications. Calibration devices are NIST-calibrated silicon photodiodes and a Laser Probe RS-5900 electrically-calibrated pyroelectric radiometer calibrated by the manufacturer with NIST traceability. Other component details are available from the author.

PROCEDURES

To determine a device's spectral responsivity, one must know the power or irradiance reaching the test device at each wavelength and the current produced by the device at each of those wavelengths. In this system, the power is measured with a calibrated photodiode or a pyroelectric radiometer. At the same time, the current produced by the monitor photodiode is measured. The computer controlling the system records the ratio of these two quantities for later use when the test device's response is measured.

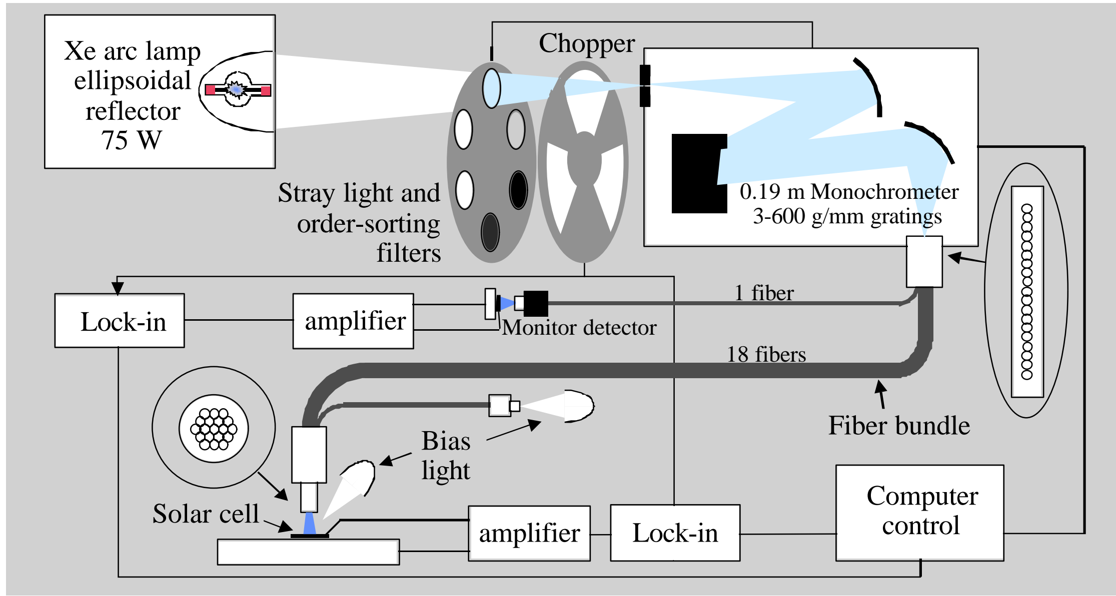

FIGURE 1. Equipment configuration for spectral responsivity measurement system.

TABLE 1. System Specifications

Item	**Specification**	**Notes**
Spectral range	280-1330	no light bias
Spectral resolution	2 nm	monochromatic beam spectral bandwidth
Spectral step size	0.14 nm	minimum
Uncertainty	≤3%	310-1060 nm, no light bias
	≤10%	< 310 nm, >1060 nm, no light bias
Wavelength uncertainty	±2 nm	
Beam size	1.6-mm diameter	minimum
Beam power	~80 µW	maximum
Beam power density	~4 mW/cm^2	0.04 "suns"
Light-bias capability	≥ 1.5 "suns"	small or apertured devices

During a test, the computer records the currents produced by the test device and the monitor photodiode at the same time for each wavelength in the test. Using the power-to-current ratio previously recorded, it converts the monitor current to a beam power quantity. The ratio of test device current $I_{TD}(\lambda)$ to beam power is the device responsivity, which is converted to units of quantum efficiency by using the monochrometer's wavelength setting λ:

$$QE(\lambda) = \frac{100\% \cdot h \cdot c \cdot I_{TD}(\lambda)}{e \cdot \lambda \cdot I_{MON}(\lambda) \cdot CV_{MON}(\lambda)}, \qquad (1)$$

where h is Planck's constant, c is the speed of light, e is the electron charge, $I_{MON}(\lambda)$ is the monitor-cell current, and $CV_{MON}(\lambda)$ is the monitor cell's calibration value in W/A units.

UNCERTAINTIES

This system estimates the uncertainties in its measurements by quantitatively combining uncertainty estimates from various sources during the measurement procedure. It specifies systematic and random components explicitly in the measurement report.

Table 2 lists the uncertainties considered for this estimation process. The uncertainty introduced during system calibration depends on the reference device used. The pyroelectric radiometer has uncertainty in the factor applied to correct its readings because the chopped waveform is not square, in its electrical–optical equivalence, in its amplifier gain, and in its analog-to-digital converter. The estimate treats as random uncertainties the drift in instrumentation gain during the measurement and the potential gain or detector nonlinearities because they change during the calibration as signal levels vary.

TABLE 2. Uncertainty Estimates

Source	Bias	Random
Calibration – pyroelectric radiometer	2%	2% + as measured
Calibration – photodiode	0.2-4.4% + 1%	1% + as measured
Measurement	1%	1% + as measured

The photodiode calibration report from NIST (2) provides uncertainty estimates for each wavelength with the spectral responsivity data. The software combines these with an additional estimate to account for other uncertainties, including the effect of multiple light reflections between the photodiode and the beam-delivery optics. Uncertainties are combined with the root-sum-square method for the 95% confidence estimate. Fixed instrumentation-gain errors do not contribute to the total uncertainty, because the same instruments are used to amplify the photodiode and test-device signals.

The computer collects multiple readings from the calibration device and monitor detector at each wavelength and computes the ratio for each reading. It combines the standard deviation of these ratios, multiplied by the appropriate student's t factor, with the random-error estimate associated with the calibration device used, to estimate the "as measured" part of the random uncertainty for the calibration shown in Table 2.

The computer combines the bias and random uncertainties in the calibration with an additional uncertainty to include the effects of wavelength uncertainty on the quantum-efficiency calculation, multiple reflections between the test device and the beam-delivery optics, and others. This result is the bias uncertainty estimate for the data report. The program estimates the measurement random uncertainty by the method described above for the calibration's random uncertainty. It combines this with an additional uncertainty to account for potential instrumentation gain-drift and nonlinearity during the test. Figure 2 illustrates the uncertainty of a measurement made using this system.

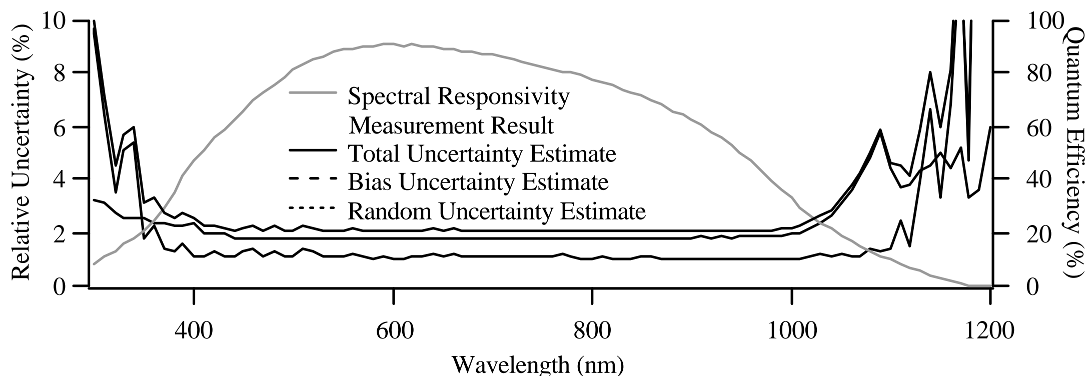

FIGURE 2. Measurement example and uncertainty estimates (24 mA/cm^2 bias light)

WAVELENGTH CALIBRATION AND SPECTRAL BANDWIDTH

Adjusting the monochrometer offsets to minimize the difference between its wavelength settings and the results of wavelength calibration checks provides the system's wavelength calibration. Calibration points are provided by line filters calibrated by NREL's CARY 5G spectrophotometer, xenon arc lamp emission lines (3), and a helium-neon laser.

Narrow-bandpass (~1-nm) filters commonly used to isolate laser wavelengths were placed over a photodiode, and the responsivity of the combination was measured. Filters with center wavelengths of 324.7, 440.7, 514.5, and 633.1 nm produced responsivity peaks within 0.8 nm of the expected wavelength. Emission lines in the system's source at 823.2, 980.0, and 992.3 nm appeared 1.2 to 1.8 nm higher than expected in the current vs. wavelength profiles of a bare photodiode's current. Light from a helium-neon laser aligned with the center of the monochrometer appeared within 0.7 nm of the expected wavelength using first-, second-, and third-order diffractions for all three gratings.

The physical positions of the monochrometer's diffraction grating, its other optical components, and the line of optical fibers simulating its exit slit determine the wavelength of the light that reaches the fiber bundle. The relative positions of these components change with temperature. In addition, position repeatability limits for the grating (the one moving part) affect the wavelength calibration. Optical properties of the gratings and fiber optics can contribute to wavelength errors. Finally, errors in the wavelength calibration sources themselves contribute to wavelength uncertainty. Rather than analytically characterize all of the known, potential error sources, an uncertainty estimate of ±2 nm is assigned to encompass these observations. Wavelength calibration errors can also affect the calculation of device quantum efficiency, as the wavelength enters the conversion from power to photon flux (see Equation 1).

Small wavelength changes can cause large changes in monochromatic beam intensity when the light source has strong emission lines and the monochrometer wavelength is set near one of those lines. The use of a monitor cell in this system enables the measurement to be relatively insensitive to such changes, as the ratio of test-cell and monitor-cell currents is used to determine the test-device responsivity.

With the helium-neon laser used in place of the xenon arc lamp source, the current vs. wavelength profile of a photodiode signal indicates that the system bandwidth is 1.4 nm, consistent with the monochrometer's design specifications. However, similar measurements across xenon emission lines and line filters indicate that the bandwidth may be slightly higher. Though this may be due to finite bandwidth of the line filters and broadening of the emission lines, the system's spectral bandwidth is specified to be ≤2 nm.

CONFIGURATION ISSUES

Light Modulation and Filters

Use of a light chopper with the monochrometer enables the lock-in amplifier to discriminate between the test-device current resulting from monochromatic light and that from stray and bias light. Order-sorting filters attenuate light that would appear at the monochrometer exit because of higher-order diffractions than the intended one. Stray-light filters attenuate light that could reach the monochrometer exit resulting from reflections from the various surfaces inside the monochrometer, including the mirrors and grating themselves.

The light chopper and filter wheel are outside the monochrometer entrance because the presence of the fiber-optic bundle prevents them from being placed at the exit. In this position, the filters reduce the total light reaching the monochrometer, thus reducing heating of the instrument. A disadvantage is that the filters get hot, changing their spectral transmittance. Delays to stabilize filter temperature are incorporated in the software to avoid errors from this problem. Heat can also damage the filters, but a broken filter does not appear to affect this system's performance.

Fiber-Optic Bundle

Common light fibers used for communication have poor transmission in the ultraviolet (UV). This system uses a fiber doped with OH^- ions to boost its UV transmission. A drawback is that the OH^- causes substantial absorption between 1340 and 1410 nm, limiting the system's continuous spectral range. The fiber's numerical aperture of 0.22 enables it to accept most of the light from the f/3.9 monochrometer.

The light fibers are linearly arranged at the bundle entrance to optically resemble a common monochrometer's output slit. Eighteen fibers convey light to the test or calibration device, where the fibers are arranged in a circle. One fiber conveys a sample of the light to the monitor cell, which functions as a calibration transfer standard. One additional fiber can convey light from a bias light source to the test

device (see Figure 1), but this method is not yet sufficiently developed. At present, a projector lamp provides bias light.

Multiple Reflections

Light reflected from the test or calibration device can, in turn, be reflected back to the device by the end of the fiber bundle. Additionally, a small amount of light exits the fiber outside the expected “cone.” The effect appears as a dependence of signal magnitude on fiber-to-device distance. To minimize this effect, a painted cap covers the ferrule holding the fibers. The paint's reflectivity is about 4%, with little spectral dependence. Even with these precautions, the signal produced by a relatively high-reflectivity photodiode varies about 1% between fiber-to-device distances of 3 and 12 mm.

BEAM POWER AND STRAY LIGHT

Figure 3 presents the spectral beam power for this system. Signal-to-noise performance and the leakage of low-level, out-of-band light through the filters and monochrometer limit measurement capability where the monochromatic beam power is lowest. Figure 4 shows that stray light is well under control in the UV and infrared regions. The left graph shows the device quantum efficiency reported, with the UV component of the monochromatic beam blocked by a 3-75 colorglass filter. The low signal levels represent the extent that stray light influences the measurement results. The right graph shows the device quantum efficiency reported in wavelength ranges for which the test device (a photodiode) should not respond.

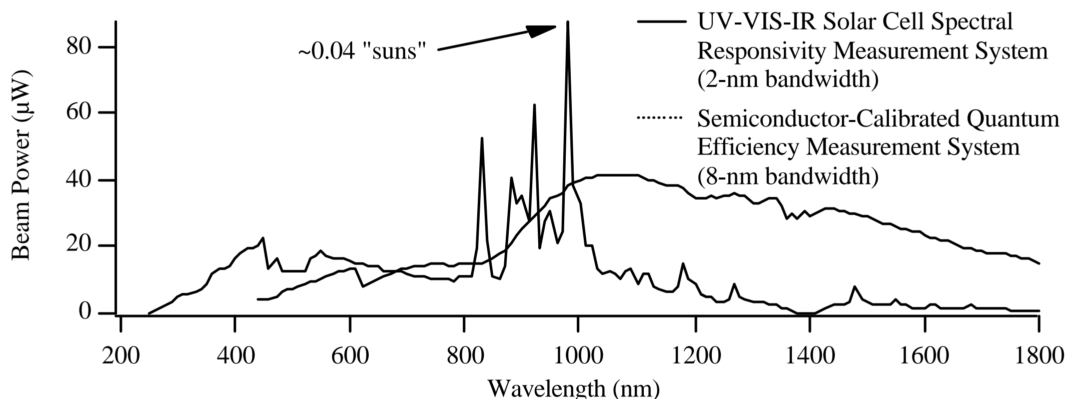

FIGURE 3. This system’s beam power is compared to that of another spectral responsivity measurement system at NREL.

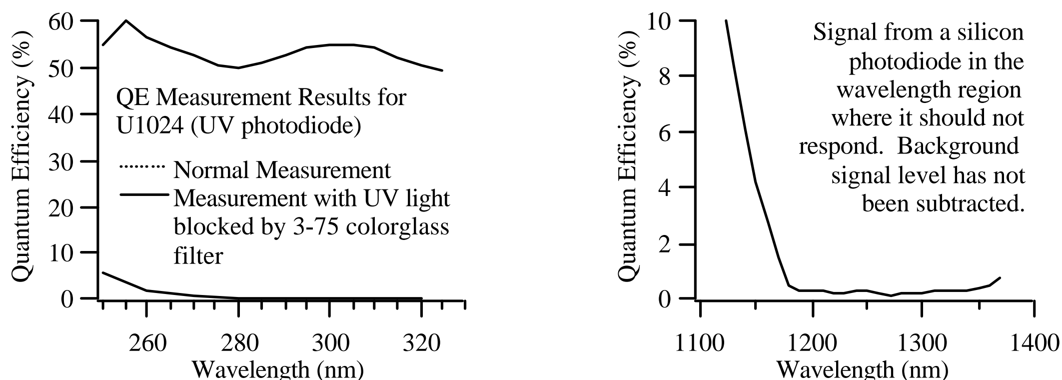

FIGURE 4. These graphs illustrate that stray light is minimal in wavelength regions where it is most likely to be a problem.

FURTHER IMPROVEMENTS

Measurements on this system, performed on request to the author by participants in DOE's PV Program, provide a valuable diversity of device characteristics and configurations, revealing opportunities for the system's continuing development. The author would appreciate feedback from potential measurement requesters on additional ideas for this list and suggestions for how to prioritize these items:

- Substitute rigorous, quantitative analysis for uncertainty judgements.
- Reduce measurement uncertainty.
- Improve wavelength calibration.
- Extend spectral range below 280 nm or above 1330 nm.
- Include uncertainty estimates in measurement reports graphically.
- Add option to measure responsivity in equal eV or wavenumber increments.
- Increase bias-light capability.
- Add temperature control for test devices.

ACKNOWLEDGEMENTS

The author thanks Ramesh Dhere of NREL for spectral transmissivity and spectral reflection measurements used to explore wavelength-calibration and multiple-reflection issues. DOE supported this work under Contract Number DE-AC36-83CH10093.

REFERENCES

1. "Standard Test Method for Determination of the Spectral Mismatch Parameter Between a Photovoltaic Device and a Photovoltaic Reference Cell [Metric]," ASTM Standard E 973M – 96, West Conshohocken, PA: American Society for Testing and Materials, 1996.

2. T.C. Larason, S.S. Bruce, A.C. Parr, *NIST Special Publication 250-41 Spectroradiometric Detector Measurements*, Washington, D.C.: U.S. Government Printing Office, 1998, pp. A-17-19. Also available at http://ois.nist.gov/sdm/

3. Weast, R., Astle, M., and Beyer, W., *CRC Handbook of Chemistry and Physics*, Boca Raton, Florida: CRC Press, Inc., 1983, pp. E-305.

TEMPERATURE AND BIAS LIGHT DEPENDENCE OF SPECTRAL RESPONSE MEASUREMENTS

H. Müllejans, H. Bossong*, E. D. Dunlop
European Commission, Joint Research Center, Institute for Environment and Sustainability, Renewable Energies Unit
TP 450, via E. Fermi 1, I-21020 Ispra (Va), Italy
Tel: +31 0332 789301, Fax: +31 0332 789268, e-mail: harald.muellejans@cec.eu.int
*Fachhochschule Trier, Fachbereich Maschinenbau und Fahrzeugtechnik
Schneidershof, D-54208 Trier, Germany, Tel: +49 651 81030, e-mail: bossongh@fh-trier.de

ABSTRACT: The aim of this work was to determine whether it is necessary to measure the spectral response of photovoltaic devices at 25°C with white bias light (as required by the international standard) or whether this requirement can be relaxed for practical purposes.

The dependence of the SR on temperature and bias light intensity was investigated for a c-Si and a thin film [$Cu(InGa)Se_2$] PV device. Two independent active temperature control devices allowed the variation of the temperature for the test device (15°C – 65°C) while maintaining the reference cell at 25°C. The bias light was provided by 24 halogen bulbs and could be adjusted in the range 0–500 W/m^2. The spectral response was then measured as a function of temperature and bias light intensity. The results show that c-Si depends more strongly on both parameters than the thin film technology. It is recommended that the spectral response be measured at a device temperature of (25 ± 2)°C for c-Si whereas temperature control is not required for the thin film device. The bias light intensity should be maintained at a minimum of 100 W/m^2 for both technologies.

Keywords: Spectral Response, Photoelectric Properties, Characterisation

1 INTRODUCTION

The IV-characteristics of PV devices are normally measured in the laboratory under standard test conditions. The results have to be corrected for the spectral mismatch, which is caused by the difference of spectral response (SR) between test device and reference cell and the differences between the simulator spectrum and the AM1.5G spectrum required by the international standard [1].

The mismatch factor required for the correction can be calculated with the SR of the test device (assuming that the simulator spectrum and the SR of the reference cell are known). According to the international standard the SR of the test device should be measured at 25°C with white bias light. This work investigates how stringent these requirements are for a first generation and a second generation device.

2 MATERIALS AND METHODS

2.1 Materials

First a monocrystalline Si cell produced with the EFG technology by ASE GmbH was tested. The same methodology was then applied to a thin film $Cu(InGa)Se_2$ mini module consisting of ten series connected cells produced by ZSW. Both devices had an area of 10cm x 10cm.

2.2 Spectral responsivity

The spectral responsivity of linear devices is independent of bias light and the measurement of the differential spectral responsivity is sufficient to determine the spectral response. For non-linear devices the differential spectral responsivity needs to be measured for different bias light levels between dark and 1000 W/m^2. The spectral response is then obtained by integrating over all bias light levels [2].

2.3 Instrumentation

A previously described set-up [3, 4] was modified and upgraded. In brief the device under test and a calibrated reference cell are placed in the measurement plane side by side and illuminated with chopped quasi monochromatic light produced by narrow bandwidth interference filters (typically 10nm FWHM) from a suitable light source. The short circuit currents of both devices are then measured via the lock-in technique and the SR of the device under test calculated. The devices can be simultaneously illuminated by 24 50W Halogen bulbs providing bias light intensities adjustable in the range 0-500 W/m^2.

The light source was changed to a solar simulator containing a steady-state Xe high-pressure lamp and an intensity controller for active stabilisation of the light intensity yielding a stability of better than 0.5% during a typically test lasting for 30 minutes. The spatial uniformity of the illumination in the measurement plane was improved by modifications to the optical lens system, finally meeting the requirement for a class A solar simulator (spatial non-uniformity better than ±2% for all wavelengths) for an area of 24cm x 14cm. Two active temperature controllers were installed to independently control the temperature of the device under test and the reference cell. For the test device the temperature controller was connected to a 20cm x 20cm large brass plate, which also contains a connection to a vacuum pump to hold the test device in place.

The ASPIRE010 cell was calibrated (against secondary reference cell PX201C from WPVS) as a dedicated reference cell for this set-up. During calibration the ASPIRE010 cell was placed exactly were it was later placed for all measurements, whereas the PX201C cell was placed at the position where the test devices were placed. This method eliminates contributions of spatial non-uniformity of the illumination for devices of sizes equal to the PX201C cell. A component remains because the test devices investigated here had a larger area. This residual non-uniformity was determined to contribute a systematic error of –1%. The ASPIRE010 cell was chosen because it has a high SR over the range 300-1200 nm, integrated channels for the cooling medium and a PT100 attached close to the junction to measure its

temperature.

The temperature of the reference cell was held at 25°C for all experiments. The reference cell is a linear device and therefore its measured differential spectral responsivity equals its spectral response.

The temperature of the test devices was varied in steps of 10K between 15°C and 65°C. The temperature was determined by the open circuit voltage method in the following way. The brass plate was heated to a certain temperature without any bias light. It was assumed that the junction temperature was equal to the temperature of the plate after thermal equilibrium was reached (ca. 30 minutes). The bias light was then switched on at maximum intensity (ca. 500 W/m^2) and the open circuit voltage measured. The peak value was measured after 2-3 sec (necessary for the lamps to reach full power) and started decaying due to the rising junction temperature. The measured peak value of the open circuit voltage was taken as the open circuit voltage of the device at that temperature and the temperature controller was adjusted to reach this value under continuous bias light at maximum intensity. The settings of the temperature controller for bias light intensities between these two extremes (dark and maximum bias light) were interpolated linearly.

The short circuit currents of the devices were measured via the potential across high precision (±0.1%) shunt resistances. This introduces a systematic deviation from the short circuit current which was determined via simulation. From the separately measured IV-curve the shunt and series resistance of the devices were determined by the program IV-fit [5]. From this the deviation between the measured current and the short circuit current of the device were determined for various bias light levels. The shunt resistance was chosen so that the deviation was identical for all bias light levels. For the ASPIRE010 cell the chosen shunt was 1 Ω, giving deviations of less than –0.002%. For the c-Si cell the shunt was 100 mΩ, giving a systematic deviation of -0.7%. For the thin film module the influence of the shunt was neglected because of its (relative) high voltage and low current.

2.4 Data analysis

From the measured SR the short circuit current was calculated as the integral over wavelength (300-1200nm) of its product with a spectrum. Three spectra were used, the AM1.5G according to the international standard [1], the spectrum of the WACOM steady-state dual lamp solar simulator and the spectrum of the PASAN pulsed large area solar simulator, both installed at the European Solar Test Installation of the Joint Research Centre.

Furthermore the mismatch factor as the ratio of the so calculated currents for a simulator spectrum to the calculated short circuit current under AM1.5G was calculated. It should be noted that this is not the full mismatch factor as is commonly used to correct the IV-curves measured on a solar simulator using a reference cell. However, here we were only interested in the changes of the mismatch factor due to temperature and bias light changes, which are entirely determined by the ratio calculated here as the reference cell is assumed to be linear (no bias light dependence) and always at 25°C.

Apart from the systematic errors due to shunt resistance and residual spatial non-uniformity mentioned above, the statistical (random) uncertainties of the measurement were determined for each measurement point and propagated through the calculation of the short circuit current and mismatch factor.

3 RESULTS

3.1 Bias light dependence

Fig. 1 shows an increase in SR of Si with increasing bias light intensity at a constant temperature of 25°C. The calculated short circuit current increases with bias light intensity up to 200 W/m^2, and then remains constant or slightly decreases (Fig. 2). Similarly the mismatch factor rises up to 100 W/m^2 and then remains constant for higher bias light intensities (Fig. 3). Similar results were obtained at a temperature of 55°C (SR not shown).

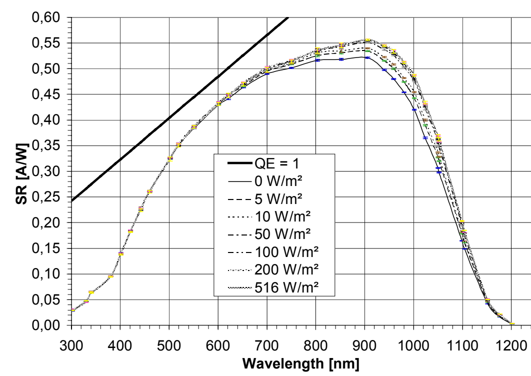

Figure 1: Bias light dependence of SR of a c-Si solar cell at constant temperature of 25°C.

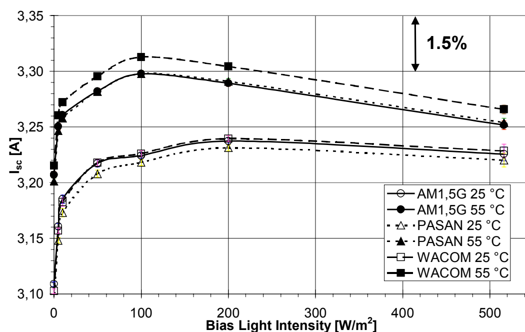

Figure 2: Bias light dependence of short circuit current calculated for three different spectra from SR measured at two temperatures (25°C and 55°C).

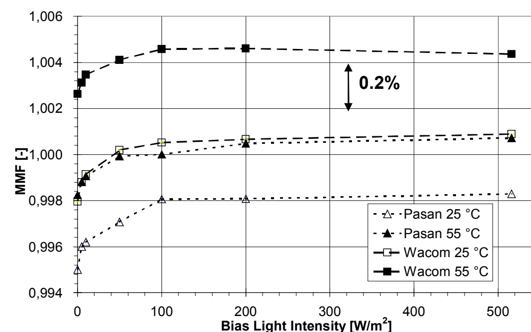

Figure 3: Bias light dependence of mismatch factor calculated for two solar simulator spectra from SR measured at two temperatures (25°C and 55°C).

The SR of the thin film module remains essentially unchanged as the bias light is increased from dark to maximum (Fig. 4). The calculated short circuit current rises initially and then falls with increasing bias light (Fig. 5) whereas the mismatch factor remains constant after an initial rise below 10 W/m^2 (Fig. 6).

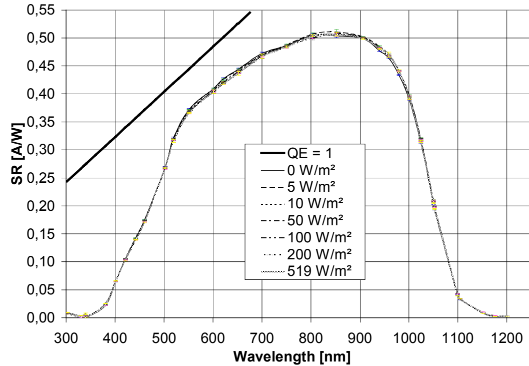

Figure 4: Bias light dependence of SR of a thin film mini-module at constant temperature of 25°C.

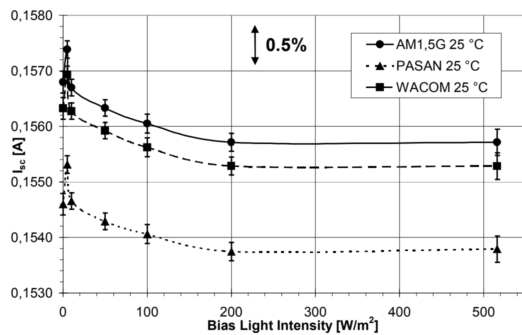

Figure 5: Bias light dependence of short circuit current calculated for three different spectra from SR measured at 25°C.

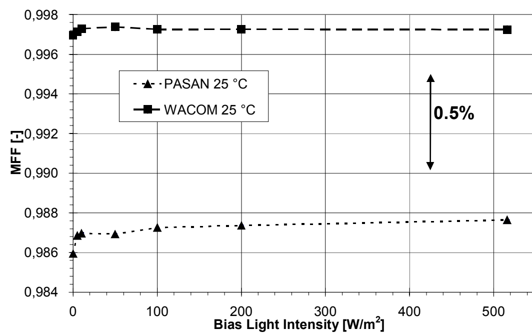

Figure 6: Bias light dependence of mismatch factor calculated for two solar simulator spectra from SR measured at 25°C.

3.2 Temperature dependence

Fig. 7 shows an increase in SR of Si with increasing temperature without bias light. The calculated short circuit current (Fig. 8) and the mismatch factor (Fig. 9) increase linearly with temperature. Similar results were obtained at a maximum bias light (500 W/m^2) with all the changes less pronounced (SR not shown).

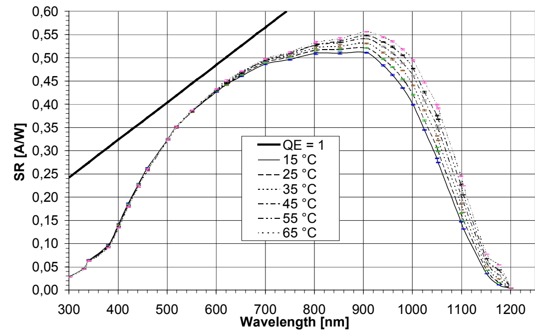

Figure 7: Temperature dependence of SR of a c-Si solar cell without bias light.

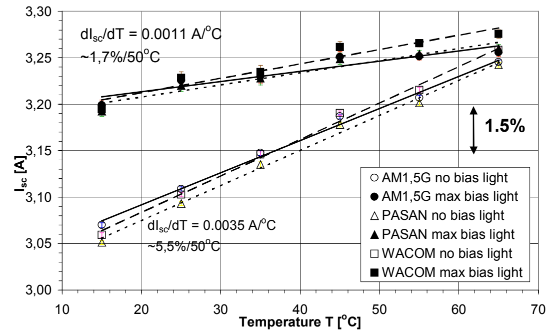

Figure 8: Temperature dependence of short circuit current calculated for three different spectra from SR measured in the dark and with 500 W/m^2 bias light.

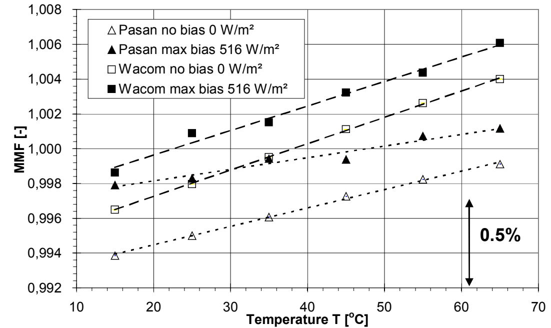

Figure 9: Temperature dependence of mismatch factor calculated for two solar simulator spectra from SR measured in the dark and with 500 W/m^2 bias light.

The SR without bias light of the thin film module remains essentially unchanged as the temperature is increased (Fig. 10). The calculated short circuit current decreases linearly with temperature (Fig. 11) whereas the mismatch factor increases linearly (Fig. 12). With bias light of 500 W/m^2 the SR again is unchanged (not shown) and the trends for calculated short circuit current and mismatch factor are inverted. It should be noted, however, that the changes are on a scale well below 1%.

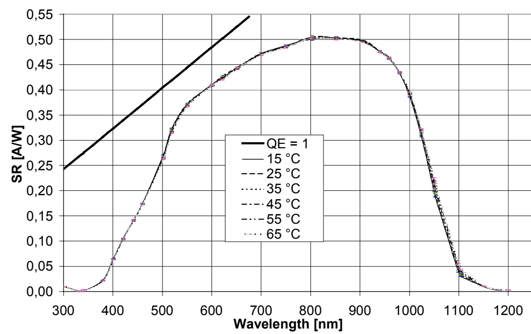

Figure 10: Temperature dependence of SR of a thin film mini-module cell without bias light.

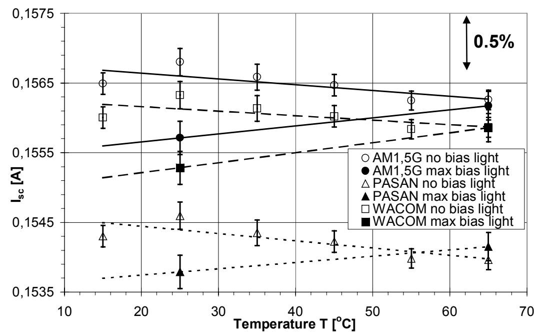

Figure 11: Temperature dependence of short circuit current calculated for three different spectra from SR measured in the dark and with 500 W/m^2 bias light.

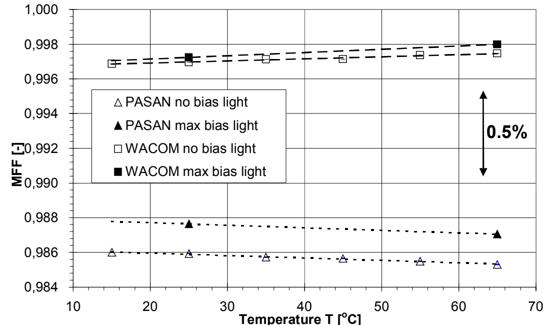

Figure 12: Temperature dependence of mismatch factor calculated for two solar simulator spectra from SR measured in the dark and with 500 W/m^2 bias light.

4 DISCUSSION AND CONCLUSIONS

The rise in SR of Si with increasing bias light can be explained by defects and impurities in the material which bind electron-hole pairs which consequently cannot contribute to the measured current [6]. As the bias light increases these centres become occupied so that all electron-hole pairs generated by the modulated monochromatic light contribute to the measured signal. The temperature dependence on the other hand is due to a decrease of the bandgap with increasing temperature and the increase in diffusion length. It is recommended to measure the SR of c-Si at a temperature of (25 ± 2)°C with a bias light intensity of 100 W/m^2. The latter replaces the requirement to measure for all bias light levels and then integrate by using a bias light level which yields an average SR and mismatch factor.

The thin film mini-module of Cu(InGa)Se$_2$ shows much less dependence of its SR on temperature and bias light intensity. Therefore the SR can be measured at any device temperature between 15°C and 65°C because this causes variations in calculated short circuit current of less than 0.3% and even less in the mismatch factor. This facilitates the measurement as temperature control is superfluous, which might be difficult to achieve on the encapsulated mini-modules. Similar arguments hold for the bias light dependence. However, it is recommended that also for this thin-film technology a bias light intensity of 100 W/m^2 is employed because of the variation in calculated short circuit current with low bias light intensities.

The statistical uncertainties in the short circuit current were typically ±0.25%. The calculated short circuit current for the WACOM simulator agreed with that actually measured within the uncertainty of 1.88% for such measurements. The uncertainties in the mismatch factor are always much smaller, because errors in the SR cancel almost entirely.

Caution should be exercised to take the results presented here as generally applicable to the two technologies. While for c-Si (probably including poly-crystalline Si) it can be expected that the behaviour is similar, for the thin film technology a greater variation in the behaviour between manufactures is expected as the properties depend critically on stoichiometry and processing. The above statements should be verified for each type before embarking on extended measuements.

5 REFERENCES

[1] IEC 60904-3.
[2] A. Schönecker, Messung der spektralen Empfindlichkeit an Hochleistunssolarzellen, Dissertation, Universität Freiburg (1994).
[3] B. Ebner, G. Agostinelli, E.D. Dunlop, Proc. 16th European Photovoltaic Solar Energy Conference, (2000) .
[4] B. Ebner, Photovoltaic Device Characterisation, Diploma Thesis, FH München (1999).
[5] IV-fit can be downloaded from the ECN webpage at http://www.ecn.nl/solar/index.html.
[6] M. A. Green, Solar Cells, Prentice Hall, Englewood Cliffs (1986).

6 ACKNOWLEDGEMENTS

We thank RWE Solar GmbH, Alzenau, Germany, and Zentrum für Sonnenenergie- und Wasserstoff-Forschung, Stuttgart, Germany, for providing the test devices and the EC-JRC for supporting this work within its institutional programme.

ADVANCED FUNCTIONAL MATERIALS

DOI: 10.1002/adfm.200600489

Accurate Measurement and Characterization of Organic Solar Cells**

By *Vishal Shrotriya*, *Gang Li*, *Yan Yao*, *Tom Moriarty*, *Keith Emery*,* and *Yang Yang**

Methods to accurately measure the current–voltage characteristics of organic solar cells under standard reporting conditions are presented. Four types of organic test cells and two types of silicon reference cells (unfiltered and with a KG5 color filter) are selected to calculate spectral-mismatch factors for different test-cell/reference-cell combinations. The test devices include both polymer/fullerene-based bulk-heterojunction solar cells and small-molecule-based heterojunction solar cells. The spectral responsivities of test cells are measured as per American Society for Testing and Materials Standard E1021, and their dependence on light-bias intensity is reported. The current–voltage curves are measured under 100 mW cm^{-2} standard AM 1.5 G (AM: air mass) spectrum (International Electrotechnical Commission 69094-1) generated from a source set with a reference cell and corrected for spectral error.

1. Introduction

Organic solar cells have attracted much attention in the last several years and today are considered a promising source for clean and renewable energy.[1–6] Organic solar cells are divided into two main categories: ones based on conjugated polymers are the so-called bulk-heterojunction (BHJ) solar cells,[7,8] and the others based on small organic molecules are bilayer heterojunction structures.[9] In polymer-based BHJ solar cells, the most common donor polymers that have been used in the past are poly[2-methoxy-5-(3,7-dimethyloctyloxy)-1,4-phenylene vinylene] (MDMO-PPV),[10–12] regioregular poly(3-hexylthiophene) (RR-P3HT),[13–20] and poly[2-methoxy-5-(2′-ethylhexyoxy)-1,4-phenylene vinylene] (MEH-PPV).[7,21,22] The most common candidate for the acceptor material is [6,6]-phenyl C_{61}-butyric acid methyl ester (PCBM).[23] On the other hand, several small molecules such as copper phthalocyanine (CuPc),[24–26] zinc pthalocyanine (ZnPc),[27,28] tetracene,[29] and pentacene[30] have been used as donors combined with buckminsterfullerene (C_{60}) molecules in a bilayer heterojunction. The highest power conversion efficiency (PCE) reported so far for polymer BHJ solar cells is close to 5 %, for devices based on P3HT.[18–20] For small-molecule-based solar cells, efficiencies up to 6.0 % have been reported for devices based on CuPc.[25] As a result of continuing research efforts, the efficiencies of organic solar cells are now fast approaching the levels where they could be put into commercial applications. For the healthy development of this technology, it is now critical to accurately determine the efficiency values to enable a fair comparison of results from different research groups. Significant efforts have been made in the past to accurately determine the efficiency of solar cells, and a standard test method has been established.[31–33] In 1980 the Cell Performance Laboratory was established by the US Department of Energy at the National Renewable Energy Laboratory (NREL) to provide the US terrestrial photovoltaics community with standardized efficiency measurement and reference-cell calibrations. In the early 1980s similar laboratories were being set up in Germany, Japan, and elsewhere. In the 1980s US and international standards were developed and adopted by the national photovoltaic (PV) calibration laboratories around the world.[32,33] Unfortunately, for organic solar cells, these internationally accepted norms are seldom followed at the research level, partially due to lack of awareness of these norms, limited resources, and/or relatively low efficiency. As a result, efficiency values under various testing conditions have been reported, which makes reliable comparison between data from different research groups very difficult. Some efforts in the past have sought to motivate the organic-solar-cell community toward adopting standards for accurately measuring efficiency.[34,35] In this paper, the research group at the University of California, Los Angeles has collaborated with the NREL to present a simple method to accurately determine the efficiency of organic solar cells. Different kinds of test-cell/reference-cell combinations have been used to calculate the spectral-mismatch factors under the standard refer-

[*] Dr. K. Emery, T. Moriarty
National Renewable Energy Laboratory
Golden, CO 80401 (USA)
E-mail: keith_emery@nrel.gov
Prof. Y. Yang, V. Shrotriya, Dr. G. Li, Y. Yao
Department of Materials Science and Engineering
University of California, Los Angeles
Los Angeles, CA 90095 (USA)
E-mail: yangy@ucla.edu

[**] V. Shrotriya and G. Li contributed equally to this work. The authors thank Douglas Sievers for helpful technical discussions. We also thank Dr. Chih-Wei Chu for helping us with device fabrication. The financial support for this research work was provided by the Office of Naval Research (N00014-01-1-0136, Program Manager Dr. Paul Armistead), and the Air Force Office of Scientific Research (F49620-03-1-0101, Program Manager Dr. Charles Lee). The work by NREL coauthors was performed under DOE contract DE-AC36-99-GO10337.

 WILEY InterScience DISCOVER SOMETHING GREAT

© 2006 WILEY-VCH Verlag GmbH & Co. KGaA, Weinheim

ence spectrum. The importance of choosing a suitable reference cell for light-source intensity calibration is also demonstrated. The spectral responsivity measurements are performed on various types of test cells, and the effect of light-bias intensity on external quantum efficiency of organic solar cells is discussed.

2. Rating Organic-Solar-Cell Performance

In this manuscript two types of organic solar cells are focused on for the purpose of accurate efficiency measurement and characterization: i) polymer/fullerene BHJ cells and ii) small-organic-molecule-based bilayer cells. Typical device structures of the two types of cells are shown in Figure 1. Also shown are the chemical structures of the active materials used in the study. The details of the fabrication procedure for both the polymer as well as the small-molecule-based PV cell are provided in the Experimental section. Two different P3HT:PCBM blend solutions were prepared—one with a 1:1 weight ratio (20 $mg\,mL^{-1}$ P3HT) in 1,2-dichlorobenzene (DCB) and one with a 1:0.8 weight ratio (10 $mg\,mL^{-1}$ P3HT) in chlorobenzene (CB)—to fabricate two types of polymer BHJ devices named P3HT:PCBM(DCB) and P3HT:PCBM(CB), respectively. Polymer BHJ solar cells using MEH-PPV were also fabricated. For small-molecule-based devices, CuPc was selected as the active layer. The encapsulated devices were brought to NREL to test their current–voltage (I–V) characteristics and measure their external quantum efficiency (EQE) values.

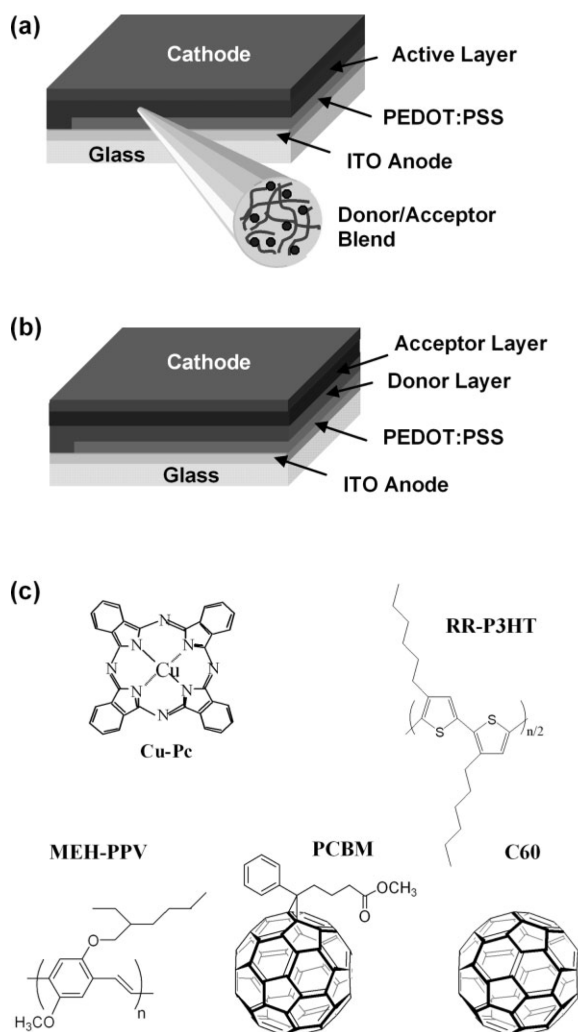

Figure 1. Typical device structures of the a) polymer/fullerene BHJ solar cell and b) small-molecule donor–acceptor heterojunction solar cell (PEDOT: poly(3,4-ethylenedioxythiophene); PSS: poly(styrene sulfonic acid); ITO: indium tin oxide). c) Chemical structures of the active materials used in this work.

The performance of PV cells is commonly rated in terms of their efficiency with respect to standard reporting conditions (SRC) defined by temperature, spectral irradiance, and total irradiance.[33] The SRC for rating the performance of terrestrial PV cells are the following: 1000 $W\,m^{-2}$ irradiance, AM 1.5 (AM: air mass) global reference spectrum, and 25 °C cell temperature.[36–40] The PCE (η) of a PV cell is given as

$$\eta = \frac{P_{\max}}{E_{\mathrm{tot}}\, A} 100 \tag{1}$$

where $P_{\max}$ is the measured peak power of the cell, A is the device area, and E_{tot} is the total incident irradiance. For Equation 1 to give a unique efficiency, E_{tot} must be with respect to a reference spectral irradiance. The current reference spectrum adopted by the international terrestrial photovoltaics community is given in International Electrotechnical Commission (IEC) Standard 60904-3 and American Society for Testing and Materials (ASTM) Standard G159.[36,38] A recent improvement to this spectrum is given in ASTM Standard G173 and is expected to be adopted by the international photovoltaics community in the next year or two.[39] The irradiance incident on the PV cell is typically measured with a reference cell. For I–V measurements with respect to a reference spectrum, there is a spectral error in the measured short-circuit current (I_{SC}) of the PV cell because of the following two reasons: i) the spectral irradiance of the light source does not match the reference spectrum, which is computer generated, and ii) the spectral responses of the reference detector and test cell are different. This error can be derived based upon the assumption that the photocurrent is the integral of the product of cell responsivity and incident spectral irradiance. This error can be expressed as spectral mismatch correction factor (M),[41,42]

$$M = \frac{\int_{\lambda_1}^{\lambda_2} E_{\mathrm{Ref}}(\lambda) S_{\mathrm{R}}(\lambda) \mathrm{d}\lambda}{\int_{\lambda_1}^{\lambda_2} E_{\mathrm{Ref}}(\lambda) S_{\mathrm{T}}(\lambda) \mathrm{d}\lambda} \frac{\int_{\lambda_1}^{\lambda_2} E_{\mathrm{S}}(\lambda) S_{\mathrm{T}}(\lambda) \mathrm{d}\lambda}{\int_{\lambda_1}^{\lambda_2} E_{\mathrm{S}}(\lambda) S_{\mathrm{R}}(\lambda) \mathrm{d}\lambda} \tag{2}$$

where $E_{\mathrm{Ref}}(\lambda)$ is the reference spectral irradiance, $E_{\mathrm{S}}(\lambda)$ is the source spectral irradiance, $S_{\mathrm{R}}(\lambda)$ is the spectral responsivity of the reference cell, and $S_{\mathrm{T}}(\lambda)$ is the spectral responsivity of the test cell, each as a function of wavelength (λ). The limits of integration λ_1 and λ_2 in the above equation should encompass the range of the reference cell and the test-device spectral re-

© 2006 WILEY-VCH Verlag GmbH & Co. KGaA, Weinheim

sponses, and the simulator and reference spectra should encompass λ_1 and λ_2 to avoid error.[43] A matched PV reference cell is typically used as the reference detector and a solar simulator is used as the light source to minimize the deviation of M from unity. Only the normalized values and not the absolute of $E_S(\lambda)$, $S_R(\lambda)$, and $S_T(\lambda)$ need to be measured for Equation 2. Equation 2 is valid for any thermal or PV detector or light source, provided none of the integrals are zero. In the extreme case of a laser as the light source and a thermal detector with a wavelength-independent responsivity, the uncertainty in M is dominated by the uncertainty in the spectral responsivity.

The total effective irradiance of the light source (E_{eff}), which is the total irradiance seen by the cell, can be determined from the short-circuit current of the reference cell under the source spectrum ($I^{\text{R,S}}$) from the equation

$$E_{\text{eff}} = \frac{I^{\text{R,S}} M}{CN} \quad (3)$$

where CN is the calibration number (in units of $\text{A}\,\text{W}^{-1}\,\text{m}^2$) for the instrument used to measure the incident irradiance. E_{eff} is different from E_{tot} in Equation 1, since E_{tot} usually refers to the total irradiance integrated over the entire spectrum, and not just the part of the spectrum the cell responds to. Both E_{eff} and E_{tot} are derived from integrating $E_S(\lambda)$ over an appropriate range of wavelength. The short-circuit current of a test cell ($I^{\text{T,R}}$) at the reference total irradiance (E_{Ref}) is given as[32,42]

$$I^{\text{T,R}} = \frac{I^{\text{T,S}} E_{\text{Ref}} CN}{I^{\text{R,S}} M} \quad (4)$$

where $I^{\text{T,S}}$ is the short-circuit current of a test cell measured under the source spectrum. Once M is known, the simulator is adjusted so that E_{eff} is equal to E_{Ref}, or

$$I^{\text{T,R}} = \frac{I^{\text{R,R}}\, I^{\text{T,S}}}{I^{\text{R,S}} M} \quad (5)$$

where $I^{\text{R,R}}$ is the calibrated short-circuit current of the reference cell under the reference spectrum and total irradiance. This is the standard simulator-based calibration procedure. The primary reference-cell calibration methods are described elsewhere.[33] The primary terrestrial procedures employed by the US at NREL follow Equations 1–5 with a primary absolute cavity radiometer as the reference detector, and direct normal sunlight as the source spectrum.

2.1. Spectral-Responsivity Measurements

The calibration procedure described in the above section requires the knowledge of M for a given light source and a given test-cell/reference-cell combination. This, in turn, requires the spectral irradiance of the light source and the spectral responsivities of the test and reference cells. The spectral responsivity, $S(\lambda)$, is calculated from the quantum efficiency, $QE(\lambda)$, by[33]

$$S(\lambda) = \frac{q\lambda}{hc} QE(\lambda) \quad (6)$$

where the constant term q/hc equals 8.0655×10^5 for wavelength in units of meters and $S(\lambda)$ in units of $\text{A}\,\text{W}^{-1}$. The term $QE(\lambda)$ is basically the number of electron–hole pairs generated per incident photon in the device multiplied by 100. To calculate M for various test-cell/reference-cell combinations, we selected four test cells and two reference cells. The reference cells were a monocrystalline silicon diode (Newport 818-SL) and a Schott visible-color glass-filtered (KG5 color filtered) Si diode (Hamamatsu S1133). As described in the Experimental section, the four different types of test cells had the following active layers: i) MEH-PPV:PCBM; ii) P3HT:PCBM(DCB); iii) P3HT:PCBM(CB); and iv) CuPc/C_{60}/BCP (BCP: bathocuproine). These four device structures represent the most common types of organic solar cells being investigated at various research laboratories in the world. The spectral responsivities were measured at NREL for all the test and reference cells as per ASTM Standard E1021.[44] The details of the spectral responsivity measurement system at NREL are discussed elsewhere by Emery et al.[45] It is also worthwhile noting that the spectral-responsivity measurements are typically performed at the short-circuit condition (i.e., at zero applied bias), and the relative responsivity is assumed to be the same at maximum-power and short-circuit points. The spectral responsivities of the test cells are plotted versus wavelength in Figure 2a–d under different light-bias intensities. The responsivities of all the cells show a slight dependence on light-bias intensity, although the behavior is different for different materials systems. For CuPc/C_{60}/BCP and P3HT:PCBM(CB), the responsivities show a small decrease when the light-bias intensity is increased from 0 to about 1 sun. On the other hand, the responsivities show a small increase for MEHPPV:PCBM- and P3HT:PCBM(DCB)-based cells with increasing light-bias intensity. However, the light-bias dependence of the responsivity for all the test cells is constant with respect to wavelength, which suggests that the mismatch-factor calculation will be independent of light-bias intensity. It has been reported earlier that the EQE shows a significant reduction when flooded with white light in organic PV cells.[24] The reduction in EQE was attributed to the increased carrier concentration under illumination, which increases recombination and hinders carrier transport due to space-charge build-up within the BHJ structure. The relatively weak dependence of EQE on light-bias intensity for all four types of devices in this work indicates that the carrier transport in the devices is not limited by space-charge build-up.

One important factor that has to be considered when measuring the spectral response of the PV device is the response time of the cell to the chopped light. For some PV cells, such as dye-sensitized solar cells (DSSCs), slow response of the device can result in a significant change in quantum efficiency with chopping frequency, and very low frequencies are required.[46]

© 2006 WILEY-VCH Verlag GmbH & Co. KGaA, Weinheim

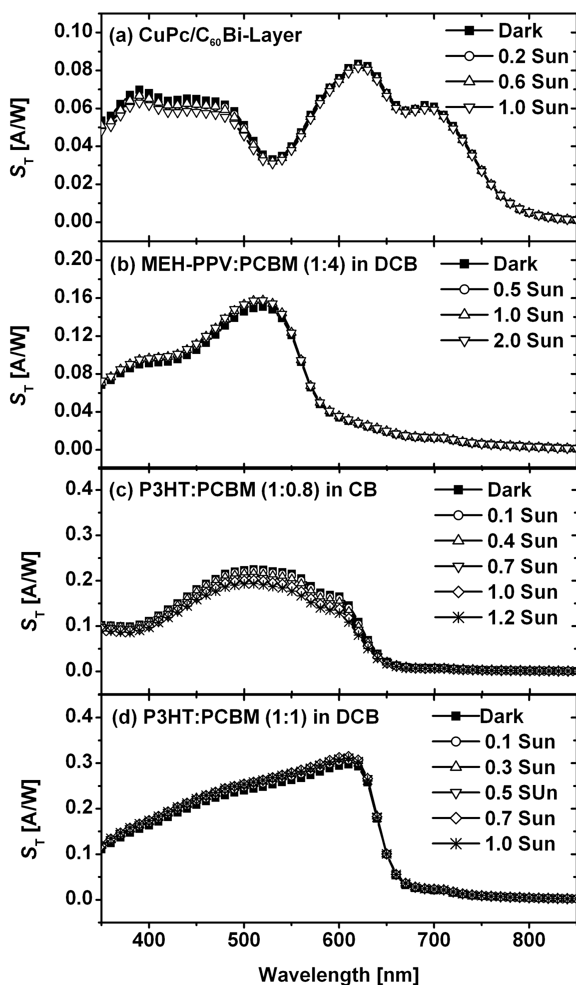

Figure 2. Spectral responsivity, $S_T(\lambda)$, under varying light-bias intensities for test cells with the following active layers: a) CuPc/C_{60}/BCP, b) MEH-PPV:PCBM, c) P3HT:PCBM(CB), and d) P3HT:PCBM(DCB).

However, for polymer solar cells, the response of the device to the incident light is very fast. As shown in Figure 3, for a P3HT:PCBM(DCB) device, the response time is less than a millisecond. As a result, all the cells responded well with chopping frequencies over 150 Hz. These results are in contrast to DSSCs, where EQE measurements are greatly affected by light-bias intensity and chopping frequency. The spectral responsivity measurements and *I–V* characterization of DSSCs has been discussed earlier by Sommeling et al.[46] and Ito et al.[47] Although they are a type of organic solar cell, DSSCs are excluded from discussion in this work, which focuses on solid-state organic solar cells.

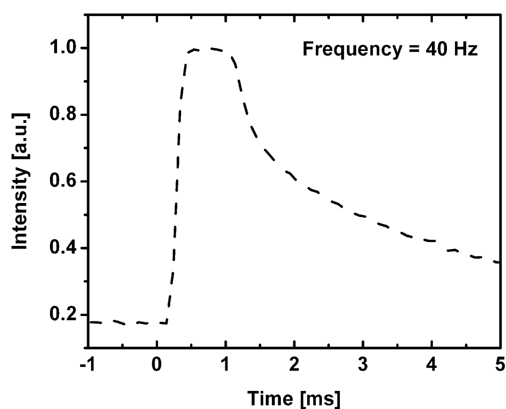

Figure 3. The response of a P3HT:PCBM(DCB) solar cell at a frequency of 40 Hz. At this frequency, the response time of the device is less than a millisecond.

2.2. Light-Source Calibration and Spectral-Mismatch Factor

The relative spectral responsivities of the test and reference cells are an important factor in the solar-simulator calibration procedure. Typically, for crystalline solar cells, the reference cell is made of the same materials and technology as the test device, which results in *M* being close to unity. Of primary importance in a reference cell is the stability in the reference cell's calibration value. For this reason most thin-film organic and inorganic devices use a Si reference cell that may have a filter to improve the spectral match. However, for polymer and small-molecule organic solar cells, it is extremely difficult to fabricate reference cells from the same materials. The reasons for this are the relatively underdeveloped fabrication techniques that lack consistent reproducibility, and poor lifetimes of these devices. Therefore, for the purpose of light-source calibration for organic-solar-cell testing, it is important to select a reference cell whose spectral response matches that of the actual test cells as closely as possible in order to minimize the spectral error that is not being numerically corrected for. The spectral responsivities of the two reference cells we selected are shown in Figure 4a. Also shown for comparison is the spectral response of a thermal detector with a quantum efficiency of unity, which is independent of the wavelength. The response of a thermal detector is very different from that of a PV cell. The unfiltered Si diode shows significant response in the wavelength range 400–1100 nm. However, the response of the Si diode with the KG5 color filter is exhibited in the wavelength range 350–700 nm. Clearly, the responsivity of the latter is similar to the responsivity of our test cells, making it more suitable for use in calibrating the light intensity of the solar simulator. This argument is further supported by calculating the mismatch factor for the four different test cells, using both the reference cells. For the purpose of calculating *M* under AM 1.5 G standard conditions, the reference spectrum used is the AM 1.5 G standard spectrum (IEC 60904),[37] and the source irradiance spectrum is the typical irradiance spectrum of the Oriel 150 W solar simulator with an AM 1.5 G filter (obtained from Newport Corporation). The reference and the source spectra used for calculating *M* are shown in Figure 4b. It should be noted that the spectra of the light sources depend on a number of factors, and the actual irradiance of the light source may be different from the typical spectrum that is shown here. The factors that can affect the irradiance spectrum of the light source are the age of the lamp, optical setting of that particular lamp, and current through the lamp. However, the aim here is to obtain "typical" spectral mismatch-factor values for different test-cell/

© 2006 WILEY-VCH Verlag GmbH & Co. KGaA, Weinheim

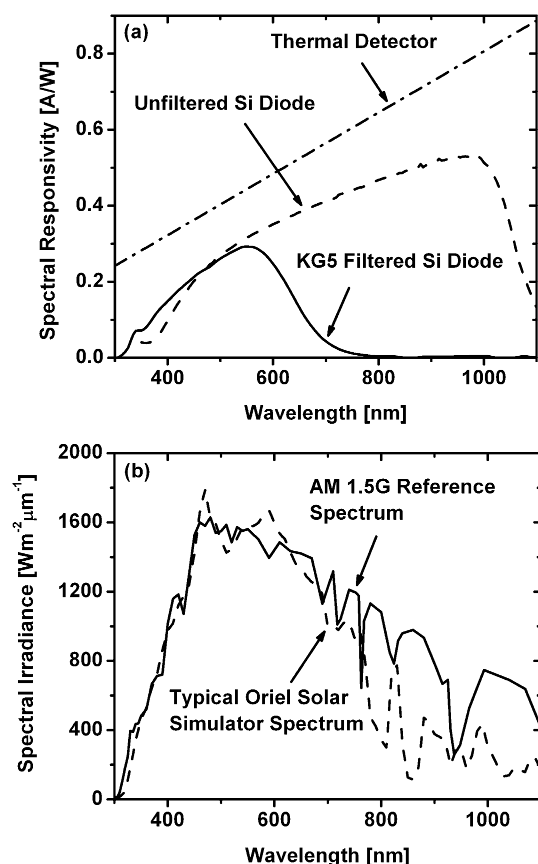

Figure 4. a) Spectral responsivities of two types of reference cells: an unfiltered monocrystalline Si diode and a Si diode with a KG5 color filter. Also shown for comparison is the spectral responsivity for a thermal detector whose quantum efficiency is unity, independent of the wavelength. b) Spectral irradiance data for AM 1.5 G reference spectrum (IEC 60904) [37] and the typical source irradiance for an Oriel 150 W solar simulator with AM 1.5 G filters (obtained from Newport Corporation). Both spectra are plotted for intensities normalized to 100 mW cm^{-2}.

reference-cell combinations using a generic-source spectral irradiance. Obviously, the most accurate M values will be obtained when the actual irradiance spectra of the source is used. The procedure described here is the general method, and the actual irradiance spectra of the source lamp as well as the actual spectral responsivities should be used to calculate the exact M value for a particular test-cell/reference-cell combination. The M values calculated by using the spectral-responsivity data for different test-cell/reference-cell combinations are summarized in Table 1. Using a Si diode with a KG5 color filter as a reference cell for light-source calibration clearly has an advantage over an unfiltered Si diode and a thermal detector. The mismatch-factor values are very close to unity when using a KG5-filtered Si diode reference cell, whereas the mismatch is 31–35 % for the unfiltered Si diode and 33–37 % for the thermal detector. This suggests that when an unfiltered Si diode or a thermal detector is used for calibrating the light-source intensity, possible errors due to spectral mismatch can be as high as 37 %. Once M is known for a specific test-cell/reference-cell combination under the source spectrum, the short-circuit current of the test device under the reference spectrum can be calculated from Equation 4 or 5. In organic solar cells that are not limited by space-charge, such as the ones we have demonstrated here, a linear dependence of short-circuit current density (J_{SC}) with incident-light intensity (I) is observed.[48] On the other hand, the open-circuit voltage (V_{OC}) and fill factor (FF) depend much more weakly on I.[49,50] However, there are bound to be several novel devices that do show a space-charge-limited effect, or other mechanism such as recombination rates, that vary nonlinearly with illumination intensity. Therefore, in order to minimize the error in efficiency calculation, it is extremely important to have M close to unity. Using a reference cell that has a spectral response similar to that of the test cells will result in minimal mismatch. For the KG5 color-filtered reference cell, the mismatch was within ±2 % for all the four test cells in this study. Mismatch factors have been used in the past to correct the efficiency values for polymer BHJ solar cells.[11,12,35] We mentioned earlier that the actual irradiance of a light source depends on several factors, one of which is the age of the lamp. As a result, the spectral mismatch would change with the age of the solar simulator's lamp. Figure 5 shows the spectral-mismatch factor for a P3HT:PCBM(DCB) test cell as a function of lamp age. The light source is a Spectrolab X25 solar simulator operating at one sun. We used two different reference cells (unfiltered and KG5-filtered Si diodes)

Table 1. Spectral-mismatch factors calculated with respect to the AM 1.5 G reference spectrum (IEC 60904) [37] for various test-cell/reference-cell combinations. The spectral responsivities of the test cells used for the data shown here were measured under a light bias of ~1 sun. The effect of light-bias intensity on the spectral-mismatch factor was negligible (< 0.1 %).

	Mismatch factors for different reference cells		
Test-cell type	KG5 color filtered	Unfiltered	Thermal detector
MEHPPV:PCBM	0.99	1.32	1.35
CuPc/C_{60}/BCP	0.98	1.31	1.33
P3HT:PCBM(CB)	1.01	1.35	1.37
P3HT:PCBM(DCB)	1.01	1.35	1.37

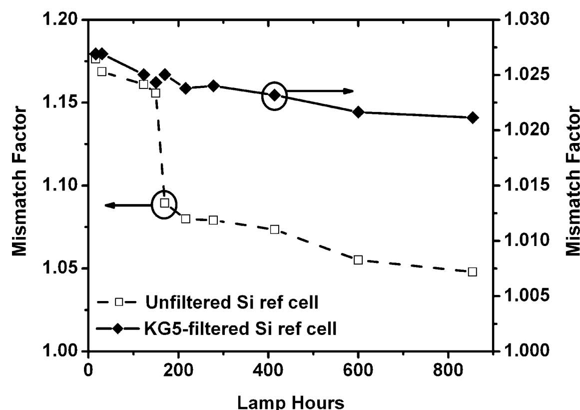

Figure 5. The change in spectral-mismatch factor as a function of lamp age for a P3HT:PCBM(DCB) test cell. The mismatch is calculated for two reference cells: unfiltered and KG5-filtered Si diodes. The light source was a one-sun Spectrolab X25 solar simulator.

© 2006 WILEY-VCH Verlag GmbH & Co. KGaA, Weinheim

for calculating M. For the unfiltered Si reference cell the mismatch varied by more than 10 % over 900 h. However, for the KG-filtered mono-Si cell, the mismatch varied by only 1 % over 900 h. This not only shows the variation in M with lamp age, but again demonstrates the advantage of using a KG5-filtered Si diode as a reference cell.

2.3. *I–V* Characteristics

The focus of this paper is on spectral-mismatch factor rather than on the device performance, because many factors, such as organic materials source, purity, and detailed device fabrication conditions, can have a significant impact on the device performance. The *I–V* curves were measured at NREL using a Spectrolab X25 solar simulator, whose intensity was set with a primary reference cell and a spectral correction factor to give the performance under the AM 1.5 global reference spectrum (IEC 60904).[37] The measurement was performed under SRC, i.e., 100 mW cm^{-2} irradiance, AM 1.5 global reference spectrum, and 25 °C cell temperature. The test cells were kept at 25.0 ± 1.0 °C during the measurement, where test cells were exposed to simulator irradiation for a measurement time of ~ 1 s. The *I–V* characteristics of the test cells are shown in Figure 6. The device area for each cell was measured using an optical microscope. The device with P3HT:PCBM(DCB) shows the best performance, with a PCE of 4.01 % (J_{SC} = 9.996 mA cm^{-2}; V_{OC} = 0.6028 V; FF = 66.60 %). However, the efficiency of the device with P3HT:PCBM(CB) is only 2.19 % (J_{SC} = 6.697 mA cm^{-2}; V_{OC} = 0.6149 V; FF = 53.14 %). Clearly, the reasons for lower performance are lower current-density and FF values, as V_{OC} is more or less unchanged. Lower J_{SC} is a result of the relatively lower EQE for the P3HT:PCBM (1:0.8) blend obtained from the CB solution, as discussed earlier (see Fig. 2). The MEHPPV:PCBM (1:4, from DCB) device has a PCE of 1.66 % (J_{SC} = 4.366 mA cm^{-2}; V_{OC} = 0.8749 V; FF = 43.46 %), and the CuPc/C_{60}/BCP device has a PCE of only 1.03 % (J_{SC} = 4.2198 mA cm^{-2}; V_{OC} = 0.5706 V; FF = 42.61 %). Even though the processing is the same, the significant difference in the performance of the two types of P3HT:PCBM devices is attributed to the morphology difference between the two active layers when spin-cast from DCB and CB. The boiling point of DCB is significantly higher than that of CB; as a result, the drying time of the film by evaporation of the solvent is slower for films spin-cast from DCB. An increased time will allow the films to achieve a higher level of ordering by self-organization of polymer chains in the active layer.[18] The obvious difference in the shape of spectral response as well as EQE of the two P3HT:PCBM-based solar cells fabricated by different methods is worth noting. The EQE of the slowly grown device has an almost constant response from 500 to 600 nm,[18] which is different from that of other reported P3HT:PCBM solar cells where EQE peaks at ca. 500 nm and consistently decreases at longer wavelengths.[15,51] The enhanced red-region spectral response is believed to be a result of improved polymer-chain ordering from the slow growth process.

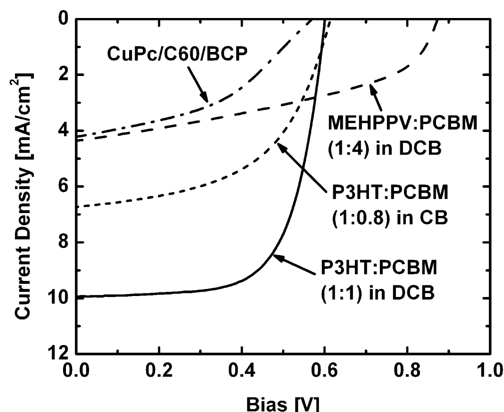

Figure 6. The *I–V* characteristics for four test cells under 100 mW cm^{-2} AM 1.5 G standard spectrum after mismatch correction.

2.4. Device Area

To accurately determine the current density through the device, it is essential to correctly measure the device area (the total frontal area of the cell including the area covered by the grids and contacts).[32,52] Usually, the device area is chosen as the area defined by the shadow mask used for evaporating the top contact. The area of the peripheral contacts to the substrate or superstrate in thin-film solar cells often exceeds the device area and is not well defined. For this reason, the peripheral thin-film contact area is not usually included as part of the total area. An important factor that can result in significant errors in the estimation of the area is the shadow effect arising from evaporating successive layers from multiple sources. One such example is the Ca/Al top electrode used in our study for all three polymer BHJ solar cells. Figure 7 shows an optical microscopy image of copper (30 nm) and gold (40 nm) metal layers successively evaporated onto an indium tin oxide (ITO) substrate. The two metals were chosen because the difference in film color makes it easier to see the shadow effect when observed under an optical microscope. For six different films prepared in this manner, the actual device area (defined by the overlapped area of the Cu and Au films) was 91 ± 3 % of the total area. It is clear that the shadow effect can therefore result

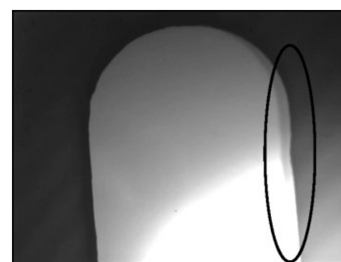

Figure 7. The grayscale optical microscope image of Cu and Au layers evaporated on an ITO substrate to demonstrate the shadow effect. The incomplete overlap of the two metallic films which results in a reduction in the device area is highlighted by the black oval.

© 2006 WILEY-VCH Verlag GmbH & Co. KGaA, Weinheim

in up to a 12 % error in current-density values. The device area for all four types of test cells that were fabricated in this study is 10.7 ± 0.2 mm^2. The device area for each cell was measured separately in order to calculate current-density and efficiency values for that device. The shadow effect can be reduced significantly by adjusting the mask orientation in such a way that the device (finger) length direction is parallel to the connecting line between the sources. The device area for each device should be measured separately to correct the values of current density.

3. Conclusions

The methods for accurately rating the performance of organic solar cells have been presented. Some of the important issues with respect to these devices were discussed, such as spectral responsivity and its behavior with light-bias intensity, dependence of the device parameters on the incident-light intensity, and calculation and application of spectral-mismatch factor for efficiency correction. Four different types of test cells and two reference cells were selected for calculating mismatch factors with respect to the AM 1.5 G reference spectrum. These typical spectral-mismatch factors provide guidance in estimating spectral mismatch in different solar-cell testing settings. The main aim of this work is to motivate the organic-solar-cell community to adopt standards similar to those used for inorganic solar cells for rating device performance.

4. Experimental

In this work, two types of organic solar cells were fabricated: polymer/fullerene BHJ and small-molecule-based bilayer solar cells. The polymer PV devices were fabricated by spin-coating a blend of polymer:fullerene sandwiched between a transparent anode and a cathode. The anode consisted of glass substrates precoated with indium tin oxide (ITO) modified by spin-coating a PEDOT:PSS layer, and the cathode consisted of Ca (ca. 25 nm) capped with Al (ca. 80 nm). Before device fabrication, the ITO (ca. 150 nm)-coated glass substrates were cleaned by ultrasonic treatment in detergent, deionized water, acetone, and isopropyl alcohol sequentially. A thin layer (ca. 25 nm) of PEDOT:PSS (Baytron P VP A1 4083) was spin-coated to modify the ITO surface. After baking at 120 °C for 1 h, the substrates were transferred inside a nitrogen-filled glove box (< 0.1 ppm O_2 and H_2O). P3HT (regioregularity 98.5 %, weight-average molecular weight, $M_w \sim 30\,000$ g mol^{-1}, purchased from Rieke Metals, Inc.; used as received) and MEH-PPV (purchased from Organic Vision, Inc.; used as received) were blended with PCBM (purchased from Nano-C, Inc.; used as received) to obtain the active layer. Two different P3HT:PCBM blend solutions were prepared—one with a 1:1 weight ratio (20 mg mL^{-1} P3HT) in DCB and one with a 1:0.8 weight ratio (10 mg mL^{-1} P3HT) in CB—to fabricate two types of devices named P3HT:PCBM(DCB) and P3HT:PCBM(CB), respectively. P3HT:PCBM(DCB) devices were fabricated by spin-coating the blend at 600 rpm for 60 s. After slow growth, the films were thermally annealed at 110 °C for 10 min in nitrogen atmosphere before evaporating the cathodes [17,18]. For P3HT:PCBM(CB) films, the spin speed was 700 rpm (60 s), and thermal annealing was done at 150 °C for 30 min post production [20]. For the MEH-PPV:PCBM devices, a solution of 1:4 weight ratio (4 mg mL^{-1} MEH-PPV) in DCB was used to spin-cast the active layer. For small-molecule-based devices, CuPc was selected as the active layer. The devices were fabricated by thermally evaporating successive layers of CuPc (20 nm), C_{60} (30 nm), BCP (10 nm), and Al (100 nm) onto the ITO/PEDOT:PSS substrates under a vacuum of 10^{-6} Torr (1 Torr ≈ 133 Pa).

Received: June 5, 2006
Final version: July 22, 2006
Published online: September 12, 2006

[1] C. J. Brabec, N. S. Sariciftci, J. C. Hummelen, *Adv. Funct. Mater.* **2001**, *11*, 15.
[2] P. Peumans, A. Yakimov, S. R. Forrest, *J. Appl. Phys.* **2003**, *93*, 3693.
[3] C. J. Brabec, V. Dyakonov, J. Parisi, N. S. Sariciftci, in *Organic Photovotlaics: Concepts and Realization*, Springer, Berlin **2003**.
[4] K. M. Coakley, M. D. McGehee, *Chem. Mater.* **2004**, *16*, 4533.
[5] C. J. Brabec, *Sol. Energy Mater. Sol. Cells* **2004**, *83*, 273.
[6] S. S. Sun, N. S. Sariciftci, in *Organic Photovoltaics: Mechanisms, Materials and Devices*, CRC Press, Boca Raton, FL **2005**.
[7] G. Yu, J. Gao, J. C. Hummelen, F. Wudl, A. J. Heeger, *Science* **1995**, *270*, 1789.
[8] N. S. Saraciftci, L. Smilowitz, A. J. Heeger, F. Wudl, *Science* **1992**, *258*, 1474.
[9] C. W. Tang, *Appl. Phys. Lett.* **1986**, *48*, 183.
[10] L. J. Lutsen, P. Adriaensens, H. Becker, A. J. Van Breemen, D. Vanderzande, J. Gelan, *Macromolecules* **1999**, *32*, 6517.
[11] S. E. Shaheen, C. J. Brabec, F. Padinger, T. Fromherz, J. C. Hummelen, N. S. Sariciftci, *Appl. Phys. Lett.* **2001**, *78*, 841.
[12] M. M. Wienk, J. M. Kroon, W. J. H. Verhees, J. Knol, J. C. Hummelen, P. A. van Hal, R. A. J. Janssen, *Angew. Chem. Int. Ed.* **2003**, *42*, 3371.
[13] T. Chen, R. D. Rieke, *J. Am. Chem. Soc.* **1992**, *114*, 10 087.
[14] R. D. McCullough, R. D. Lowe, M. Jayaraman, D. L. Anderson, *J. Org. Chem.* **1993**, *58*, 904.
[15] F. Padinger, R. S. Rittberger, N. S. Sariciftci, *Adv. Funct. Mater.* **2003**, *13*, 85.
[16] D. Chirvase, J. Parisi, J. C. Hummelen, V. Dyakonov, *Nanotechnology* **2004**, *15*, 1317.
[17] G. Li, V. Shrotriya, Y. Yao, Y. Yang, *J. Appl. Phys.* **2005**, *98*, 043 704.
[18] G. Li, V. Shrotriya, J. Huang, Y. Yao, T. Moriarty, K. Emery, Y. Yang, *Nat. Mater.* **2005**, *4*, 864.
[19] M. Reyes-Reyes, K. Kim, D. L. Carroll, *Appl. Phys. Lett.* **2005**, *87*, 083 506.
[20] W. L. Ma, C. Y. Yang, X. Gong, K. Lee, A. J. Heeger, *Adv. Funct. Mater.* **2005**, *15*, 1617.
[21] N. S. Sariciftci, D. Braun, C. Zhang, V. I. Sradnov, A. J. Heeger, G. Stucky, F. Wudl, *Appl. Phys. Lett.* **1993**, *62*, 585.
[22] S. Alem, R. de Bettignies, J.-M. Nunzi, M. Cariou, *Appl. Phys. Lett.* **2004**, *84*, 2178.
[23] J. C. Hummelen, B. W. Knight, F. LePeq, F. Wudl, J. Yao, C. L. Wilkins, *J. Org. Chem.* **1995**, *60*, 532.
[24] P. Peumans, S. Uchida, S. R. Forrest, *Nature* **2003**, *425*, 158.
[25] J. Xue, S. Uchida, B. P. Rand, S. R. Forrest, *Appl. Phys. Lett.* **2004**, *85*, 5757.
[26] F. Yang, M. Shtein, S. R. Forrest, *Nat. Mater.* **2005**, *4*, 37.
[27] J. Drechsel, B. Männig, F. Kozlowski, D. Gebeyehu, A. Werner, M. Koch, K. Leo, M. Pfeiffer, *Thin Solid Films* **2004**, *451–452*, 515.
[28] J. Drechsel, B. Männig, D. Gebeyehu, M. Pfeiffer, K. Leo, H. Hoppe, *Org. Electron.* **2004**, *5*, 175.
[29] C.-W. Chu, Y. Shao, V. Shrotriya, Y. Yang, *Appl. Phys. Lett.* **2005**, *86*, 243 506.
[30] S. Yoo, B. Domercq, B. Kippelen, *Appl. Phys. Lett.* **2004**, *85*, 5427.
[31] K. Emery, C. Osterwald, *Sol. Cells* **1986**, *17*, 253.
[32] K. Emery, C. Osterwald, in *Current Topics in Photovoltaics*, Vol. 3, Academic, London **1988**, Ch. 4.
[33] K. Emery, in *Handbook of Photovoltaic Science and Engineering* (Eds: A. Luque, S. Hegedus), Wiley, Chichester, UK **2003**, Ch. 16.
[34] J. Rostalski, D. Meissner, *Sol. Energy Mater. Sol. Cells* **2000**, *61*, 87.

© 2006 WILEY-VCH Verlag GmbH & Co. KGaA, Weinheim

[35] J. M. Kroon, M. M. Wienk, W. J. H. Verhees, J. C. Hummelen, *Thin Solid Films* **2002**, *403–404*, 223.
[36] Standard IEC 60904-3, Measurement Principles for Terrestrial PV Solar Devices with Reference Spectral Irradiance Data, International Electrotechnical Commission, Geneva, Switzerland.
[37] Standard IEC 60904-1, Photovoltaic devices Part 1: Measurement of Photovoltaic Current-Voltage Characteristics, International Electrotechnical Commission, Geneva, Switzerland.
[38] ASTM Standard G159, Standard Tables for Reference Solar Spectral Irradiances: Direct Normal and Hemispherical on 37° Tilted Surface, American Society for Testing and Materials, West Conshocken, PA, USA.
[39] ASTM Standard G173, Standard Tables for Reference Solar Spectral Irradiances: Direct Normal and Hemispherical on 37° Tilted Surface, American Society for Testing and Materials, West Conshocken, PA, USA.
[40] Standard ASTM E948, Standard Test Method for Electrical Performance of Non-Concentrator Photovoltaic Cells Using Reference Cells, American Society for Testing and Materials, West Conshocken, PA, USA.
[41] K. Emery, C. R. Osterwald, T. W. Cannon, D. R. Myers, J. Burdick, T. Glatfelter, W. Czubatyj, J. Yang, in *Proc. 18th IEEE Photovoltaic Specialist Conf.*, IEEE, New York **1985**, p. 623.
[42] C. R. Osterwald, *Sol. Cells* **1986**, *18*, 269.
[43] H. Field, K. Emery, in *Proc. 23rd IEEE Photovoltaic Specialist Conf.,* IEEE, New York **1993**, p. 1180.
[44] Standard ASTM E1021, Standard Test Methods for Measuring Spectral Response of Photovoltaic Cells, American Society for Testing and Materials, West Conshocken, PA, USA.
[45] K. Emery, D. Dunlavy, H. Field, T. Moriarty, in *Proc. 2nd World Conf. and Exhibition on Photovoltaic Solar Energy Conversion,* European Commission, **1998**, p. 2298.
[46] P. M. Sommeling, H. C. Rieffe, J. A. M. van Roosmalen, A. Schönecker, J. M. Kroon, J. A. Wienke, A. Hinsch, *Sol. Energy Mater. Sol. Cells* **2000**, *62*, 399.
[47] S. Ito, H. Matsui, K. Okada, S. Kusano, T. Kitamura, Y. Wada, S. Yanagida, *Sol. Energy Mater. Sol. Cells* **2004**, *82*, 421.
[48] L. J. A. Koster, V. D. Mihailetchi, R. Ramaker, P. W. M. Blom, *Appl. Phys. Lett.* **2005**, *86*, 123 509.
[49] V. Dyakonov, *Thin Solid Films* **2004**, *451–452*, 493.
[50] S. Yoo, B. Domercq, B. Kippelen, *J. Appl. Phys.* **2005**, *97*, 103 706.
[51] J. Y. Kim, S. H. Kim, H.-H. Lee, K. Lee, W. Ma, X. Gong, A. J. Heeger, *Adv. Mater.* **2006**, *18*, 572.
[52] Standard ASTM E1328, Standard Terminology Relating to Photovoltaic Solar Energy Conversions, American Society for Testing and Materials, West Conshocken, PA, USA.

© 2006 WILEY-VCH Verlag GmbH & Co. KGaA, Weinheim

MEASUREMENT OF MINORITY CARRIER DIFFUSION LENGTH FROM SPECTRAL RESPONSE OF THIN FILM POLYCRYSTALLINE SILICON SOLAR CELLS

R. KISHORE*

C.N.R.S. Laboratoire de Physique des Solids, 1 place A. Briand, F-92195 Meudon, and C.N.R.S. Centre d'Etudes de Chimie Métallurgique, 15 rue G. Urbain, F-94100 Vitry (France)

M. BARBE

C.N.R.S. Laboratoire de Physique des Solides, 1 place A. Briand, F-92195 Meudon (France)

J. L. PASTOL

C.N.R.S. Centre d'Etudes de Chimie Métallurgique, 15 rue G. Urbain, F-94100 Vitry (France)

M. CAYMAX

I.M.E.C. Kapeldreef 72, B-3030 Heverlee (Belgium)

J. E. BOUREE

C.N.R.S. Laboratoire de Physique des Solides, 1 place A. Briand, F-92195 Meudon (France)

G. REVEL

C.N.R.S. Centre d'Etudes de Chimie Métallurgique, 15 rue G. Urbain, F-94100 Vitry (France)

M. RODOT

C.N.R.S. Laboratoire de Physique des Solides, 1 place A. Briand, F-92195 Meudon (France)

(Received April 15, 1987; accepted January 7, 1988)

Summary

A simple model of epitaxial silicon solar cells has been used to explain their observed spectral response. This model has been applied to a series of boron-doped substrates covered by epilayers of various thicknesses and resistivities. It is concluded that the minority carrier diffusion length L_n in the thin epilayer can be determined by analyzing the long wavelength spectral response with the help of this model. It is also found that the short-

*Permanent address: National Physical Laboratory, Hillside Rd, 110012 Delhi, India.

0379-6787/88/$3.50 © Elsevier Sequoia/Printed in The Netherlands

circuit current density J_{sc} and L_n depend more on the epilayer defects induced by the defects of the heavily doped substrates than on epilayer thickness or resistivity.

---

1. Introduction

The minority carrier diffusion length L is a very important parameter for solar cell applications. Surface photovoltage (SPV) [1 - 4] and photoresponse (PR) [5 - 7] methods usually make it possible to determine the electron diffusion length L_n in the p-base of n^+p or n^+pp^+ silicon solar cells, using the following relation between L_n, the optical absorption coefficient α and the internal quantum efficiency Q

$$\frac{1}{Q} = 1 + \frac{1}{\alpha L_n} \qquad (1)$$

This relation, which is valid under certain conditions (see Section 2), shows that extrapolation from the measured $1/Q$ *vs.* $1/\alpha$ data points to $1/Q = 0$ yields an intercept on the $1/\alpha$ axis at $1/\alpha = -L_n$.

In thin film solar cells, however, where the active layer thickness may be smaller than the diffusion length L_n to be measured, some of the conditions assumed for relation (1) are violated and therefore the correct value of L_n cannot be determined from extrapolation of the $1/Q$ *vs.* $1/\alpha$ curve [8, 9]. Similarly the LBIC method, in which the value of L_n is deduced from the photocurrent of an MIS diode built on the material under investigation, cannot be applied to a thin layer as is usual for thicker materials [10].

Recently the PR method was applied [8] to characterize thin films of crystalline silicon, using a more appropriate relation between Q and L_n than relation (1). MIS diodes were specially built and Hovel's equations [11] were written for this kind of cell, assuming that the surface recombination velocity S_n at the back of the active layer was infinite and allowing for optical confinement of radiation in the film. L_n was determined by comparing the values of Q for two different wavelengths in the infrared range.

In the present study, we aimed at characterizing the thin films of crystalline silicon used in epitaxial solar cells. These cells, which were first considered by Chu and Chu [12], are designed to minimize the quantity of high purity silicon used in a polycrystalline silicon solar cell. To make them [13, 14] we deposit a thin p-epilayer on a wafer cut from a p^+ metallurgical grade (MG) silicon ingot, and build the n-type front layer, the front and back contacts and the antireflection (AR) layer by screen printing processes. This technique is potentially very cheap and already leads to 10.3% conversion efficiency. In order to optimize such cells, an important step is to determine the electron diffusion length L_n in the epilayer from measurement of the spectral response of the cell. For this purpose, use of the photoresponse method presents a further difficulty which was underlined recently by Singh

[15]: since the substrate may contribute in part to the long wavelength spectral response, it may not be easy to single out the epilayer contribution and deduce from it the value of L_n in the epilayer.

We have adapted the PR method to this special problem. In Section 2, we write Hovel's equations for the present case, *i.e.* that of a structure (Fig. 1) where: (i) both the front n layer and the back p^+ layer contribute very little to the photocurrent; (ii) the photocurrent generated in the epilayer depends on the recombination velocity S_n at the substrate/epilayer interface; (iii) no optical confinement occurs, because the back interface is an Si/Si one. Experiments fitting the conditions of validity of this model are described in Section 3. In Section 4, we give the values of L_n in the epilayers; in particular we confirm that, as is generally found [14 - 17], the epilayer thickness and resistivity influence only slightly the performance of epitaxial cells. Finally in Section 5 we discuss this latter point as well as the validity of our simple model.

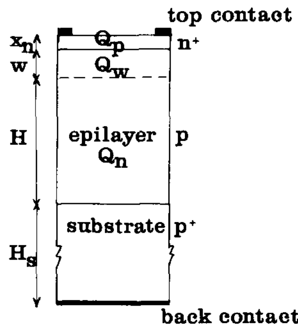

Fig. 1. Schematic diagram of thin film solar cell.

2. The model

Let us consider an n^+pp^+ cell structure as shown in Fig. 1. Let x_n, w, H and H_s be the thicknesses of the n-layer, depletion region, p-layer and p^+ substrate respectively. Let us neglect the photogeneration in the substrate, an assumption which will be discussed later in Section 5. Considering the n and p regions to have constant doping, we may define L_p and D_p to be respectively the (constant) hole diffusion length and diffusion coefficient in the n (top) region, and L_n and D_n to be respectively the (constant) electron diffusion length and diffusion coefficient in the p (epilayer) region. Then, according to Hovel [11], at a wavelength λ where the absorption coefficient is α, the contribution to the internal quantum efficiency Q of the top, depletion and epilayer regions can be written as

$$Q_p = \frac{\alpha L_p}{(\alpha L_p)^2 - 1}\left[\frac{\epsilon_p + \alpha L_p - \{\epsilon_p \cosh(x_n/L_p) + \sinh(x_n/L_p)\}\exp(-\alpha x_n)}{\epsilon_p \sinh(x_n/L_p) + \cosh(x_n/L_p)} - \alpha L_p \exp(-\alpha x_n)\right] \quad (2)$$

$$Q_w = \exp(-\alpha x_n)\{1 - \exp(-\alpha w)\} \tag{3}$$

$$Q_n = \frac{\alpha L_n}{(\alpha L_n)^2 - 1}\exp(-\alpha d) \times \left[\alpha L_n - \frac{\epsilon_n\{\cosh(H/L_n) - \exp(-\alpha H)\} + \sinh(H/L_n) + \alpha L_n \exp(-\alpha H)}{\epsilon_n \sinh(H/L_n) + \cosh(H/L_n)}\right] \tag{4}$$

Here

$$\epsilon_p = \frac{S_p L_p}{D_p}; \qquad \epsilon_n = \frac{S_n L_n}{D_n}$$

and

$$d = x_n + w \tag{5}$$

S_p is the hole recombination velocity at the interface between the n-region and the antireflection coating and S_n is the electron recombination velocity at the epilayer–substrate interface.

Using the above equations and taking the values of various parameters as given in Fig. 2, the quantum efficiency values for the three different regions were traced for different values of wavelengths in the range 0.8 - 1.05 μm. It is clear that the major contribution comes from the epilayer.

For long wavelength photons, $\exp\{-\alpha(x_n + w)\} \simeq 1$. For a thick epilayer ($H \gg L_n$, $1/\alpha$), then $\exp(-\alpha H) \to 0$ and $\sinh(H/L_n) \simeq \cosh(H/L_n) \simeq 0.5 \exp(H/L_n)$: eqn. (4) tends to the form of eqn. (1). However these approximations do not apply to typical epitaxial solar cells. On the one hand the epilayer quality may be rather high: we have quoted 62 μm in a previous paper [14]. On the other hand the optimal epilayer thickness has been determined to lie near 20 μm by other authors [16, 17]. In this case we have to rely on eqn. (4) rather than eqn. (1).

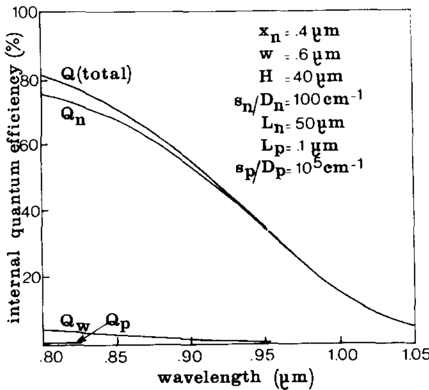

Fig. 2. Contributions to the quantum efficiency generated by the n-layer (Q_p), the space charge region (Q_w) and the thin p-layer (Q_n).

In our epitaxial cells, the front layer contribution Q_p can be almost neglected. That of the depletion layer, Q_w, has been included in expression (4) for the epilayer contribution as a small correction, by taking d as an adjustable parameter rather than one equal to $x_n + w$ as in expression (5). This allows us to take into account the front layers, not only through their absorption, but also through their small contribution to the quantum efficiency, which is nonzero over a small part (0.8 - 0.9 μm) of the wavelength range considered. In expression (4) for the quantum efficiency, the electron recombination velocity at the epilayer–substrate interface was taken to be

$$S_n \simeq \frac{P}{P_s} \frac{D_{ns}}{L_{ns}} \tag{6}$$

where P and P_s are the majority carrier concentrations in the epilayer and the substrate and D_{ns} and L_{ns} respectively the electron diffusion coefficient and the electron diffusion length in the substrate. This expression has been shown [18, 19] to describe correctly the case of an abrupt interface between the thin epilayer and a thick substrate.

Some properties of this model are illustrated by Figs. 3 and 4. Figure 3 shows, according to eqn. (4), theoretical $1/Q_n$ vs. $1/\alpha$ curves for various values of epilayer thickness H and for two limiting values of S_n: a very high value in Fig. 3(a) and a very low one in Fig. 3(b). It is seen that for $H < L_n$ the extrapolation of $1/Q_n$ *vs.* $1/\alpha$ no longer gives the values of L_n. Furthermore, Fig. 3(b) shows that, when $S_n \simeq 0$ and $H \simeq L_n$, an increase in Q may occur in a certain wavelength range due to the electron acceleration which is caused by the "back surface field" at the high–low junction. The effect of varying the diffusion length for a fixed value of λ is shown in Fig. 4; here it can be seen that the quantum efficiency is determined essentially by the epilayer quality (*i.e.* the value of L_n) only if $L_n < H$, whereas if $L_n > H$, Q is

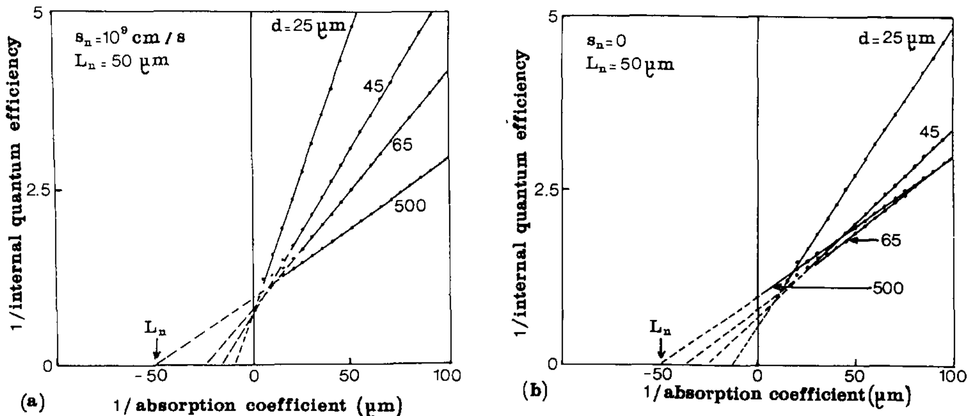

Fig. 3. Theoretical variation in internal quantum efficiency with wavelength and p-layer thickness, for fixed electron diffusion length (L_n = 50 μm) and two values of substrate–epilayer recombination velocities: (a) $S_n = 10^9$ cm s^{-1}; (b) S_n = 0 cm s^{-1}.

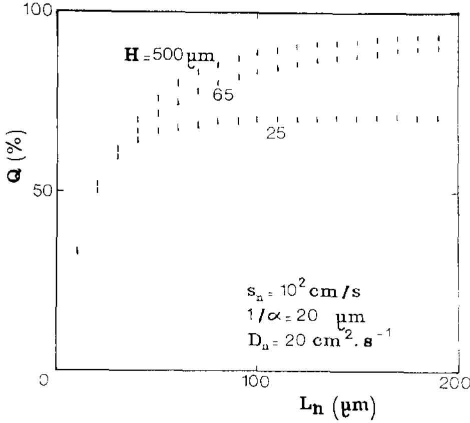

Fig. 4. Theoretical variation in internal quantum efficiency with epilayer thickness and quality, for fixed wavelength.

almost independent of epilayer quality and is determined mainly by the absorption losses in the thin epilayer.

3. Experimental details

3.1. Ingot growth and characterization

We needed highly doped substrates for two reasons, firstly to minimize the photogeneration in the substrate, and secondly to minimize the ratio P/P_s which determines the value of S_n, as shown by eqn. (6), or in other words to maximize the back surface field.

A polycrystalline silicon ingot was grown from electronic grade silicon doped heavily (12.5 μg g^{-1}) with boron, using a directional solidification method [20]. A flat-bottom silica crucible coated internally with silicon nitride powder was used as the container; its dimensions were 98 mm in height, 55 mm internal diameter and 2 mm thickness. The growth rate was kept at approximately 1 cm h^{-1}. After removing the ingot from the crucible and etching it, it was cut into vertical sections and a block of 25 × 25 mm cross-section was sliced to get 400-μm thick wafers for thin film deposition and solar cell fabrication. The slices were numbered starting from the bottom. The resistivity and carrier concentration were measured on these slices by four-probe and $C-V$ methods. The resistivity lies between 0.03 and 0.04 Ωcm and the carrier concentration between 1 and 2×10^{18} cm^{-3}, so that $D_{ps} = 3 \pm 1$ cm^2 and presumably D_{ns} is near 6 cm^2 s^{-1} [21]. The mean grain size was several mm throughout the whole ingot. Wafers near the middle of the ingot (nos. 25 - 45) were lapped and polished by chemical mechanical polishing. LBIC measurements gave L_{ns} values of 18 - 20 μm. These small values can be attributed both to a nickel contamination at the level of 8×10^{14} cm^{-3} (other metals were below the detection threshold of neutron activation analysis) and to intragrain defects (perhaps related to carbon segregation) which do appear with increasing density in slices 30 - 45.

3.2. Epilayer growth

The epilayer deposition of silicon was carried out in an ASM "cold wall" reactor, with a horizontal susceptor heated by quartz lamps. Before being placed in the furnace, the slices were treated to get a damage-free surface, using standard RCA cleaning followed by an HF dip. Pure silicon layers were deposited from SiH_2Cl_2 at 1120 °C, at a rate of 55 - 60 μm h^{-1}. Layer thickness was adjusted to between 20 and 65 μm and layer resistivity between 0.1 and 2 Ωcm using additions of B_2H_6 in the gas.

Epilayer thickness was measured according to ASTM test method F 143-73 (reapproved in 1978), which involves measurement of the dimensions of stacking faults grown in the epilayer by means of differential interference contrast microscopy. This procedure was carried out on monocrystalline test wafers of known orientations that accompanied the polycrystalline wafers during the epi-growth. The in-house reproducibility of the measurements was 5%.

3.3. Cell fabrication

Polycrystalline silicon wafers with silicon epilayers deposited on them were used to fabricate solar cells by the integral screen-printing technique described by Mertens *et al.* [22]. In this technique, the three steps — P diffusion, back and front metallization and antireflection coating — are carried out by deposition of a screen-printing paste followed by adequate annealing. This process is capable of giving reference cells (for single crystal EG-Si without epilayer) of maximum efficiency 12.5%. The completed cells, of n^+pp^+ structure with an n^+p junction at the top, were approximately 18 $\times$ 18 mm^2 in dimension; the actual cell and grid areas were measured accurately for each cell.

3.4. Spectral response measurement

The spectral response of the cells was measured using a monochromator, current-to-voltage converter and lock-in amplifier, in the wavelength range 0.4 - 1.1 μm. The cell was illuminated over its whole area. Before each measurement, a calibrated standard cell was also measured. The external quantum efficiency of each cell was deduced from the two series of data, taking into account the exact cell area (total area minus grid area). The total current density J_{sc} (integrated over the whole spectrum) was also calculated for an intensity of 100 mW cm^{-2} with an air mass (AM) 1.5 spectrum.

4. Results

Table 1 shows for each cell the substrate number, substrate resistivity, epilayer thickness and resistivity and short-circuit current density. Figure 5 shows six of the measured spectral responses over the whole range from 0.4 to 1.1 μm.

The measured quantum efficiency Q_m in the range 0.8 - 1.05 μm was then compared with the calculated value Q_c, using the model described

TABLE 1

Summary of substrate, epilayer and solar cell parameters

Substrate and cell no.	*B-doped substrate resistivity* (Ωcm)	*P-type epilayer*		J_{sc} (mA cm^{-2})	L_n (μm)
		Thickness (μm)	*Resistivity* (Ωcm)		
WBRC 3542	0.035	25	2.3	20.14	17.3
WBRC 3525	0.039	24	2.0	20.47	35.5
WBRC 3536	0.034	45	1.7	19.91	24.8
WBRK 3527	0.041	45	1.7	22.73	40.8
WBRC 3528	0.029	64	1.6	22.45	32.0
WBRC 3537	0.036	64	1.6	19.77	22.8
WBRC 3539	0.032	25	0.15	18.85	20.5
WBRK 3529	0.031	25	0.15	20.33	33.0
WBRC 3530	0.031	43	0.15	21.29	31.2
WBRC 3540	0.034	43	0.15	19.48	24.7
WBRC 3532	0.034	62	0.15	20.76	29.4
WBRK 3541	0.035	62	0.15	19.04	18.2

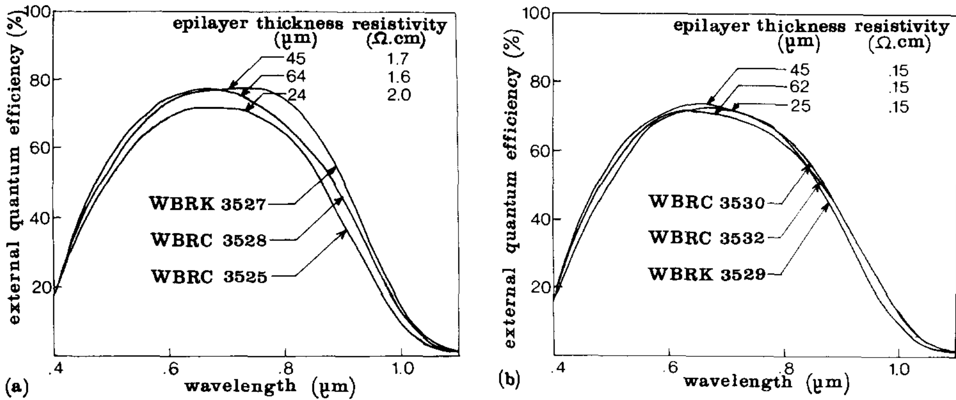

Fig. 5. Experimental solar cell spectral response: (a) for epilayer resistivity near 2 Ωcm; (b) for epilayer resistivity 0.15 Ωcm.

above together with the measured value of H and various values of the parameters d, S_n and L_n. The absorption coefficient $\alpha(\lambda)$ was taken from Swimm and Dumas [23] and the reflectivity $R(\lambda)$ was chosen to follow the curve given fór "blue cells" by Scheer and Wagemann [24]. The quality of the fit was determined from the value of $(Q_c - Q_m)/(Q_c + Q_m)$. This ratio could be minimized to reach values lower than 10^{-3} over the whole wavelength range 0.8 - 1.05 μm.

It was verified that varying d could improve the fit only in the wavelength range 0.8 - 0.9 μm, and by a small proportion; we generally chose 0.1 - 0.3 μm. The fit was more sensitive to values of S_n; for this parameter

we chose systematically the theoretical value given by eqn. (6). Using D_{ns} = 6 cm^2 s^{-1} [21] for a substrate of resistivity 0.03 Ωcm and L_{ns} = 10 μm (somewhat smaller than the measured value before cell processing to take account of the damage occurring during cell processing), and considering the variations in substrate and layer resistivity and also the fact that the interface is not strictly abrupt, we can accept $S_n \simeq 30 - 60$ cm^2 s^{-1} when the epilayer resistivity is near 1.5 Ωcm and $S_n \simeq 400 - 800$ cm^2 s^{-1} when the epilayer resistivity is near 0.15 Ωcm. We generally used S_n = 45 cm^2 s^{-1} or 600 cm^2 s^{-1} for these two cases respectively, and observed that a variation in S_n of as much as 50% of these values changed the quality of the fit only little. The fit is very sensitive to the value of H; considering the above-mentioned accuracy of epilayer thickness determination, uncertainties in H are probably the largest source of error in the determination of L_n by our method. The fact that we neglect substrate photoresponse is the second main cause of error; it is small in the present case (see Section 5) since the substrate is highly doped and should exhibit only a small photoresponse.

When d, S_n and H are chosen as explained above, the result of the fit is extremely sensitive to the value of L_n. The best fit gives the values of L_n shown in the last column of Table 1. These values, as well as those for J_{sc}, are plotted in Fig. 6 as functions of the slice number. At first inspection, there appears to be good correlation between L_n and J_{sc}, as expected.

Figure 6 shows that L_n has a tendency to decrease for increasing slice number, that is (see Section 3) for decreasing crystalline quality of the substrate.

L_n is found to change very little with epilayer thickness H. For instance, cells 42, 36 and 37 had epilayers with resistivity ρ = 2 Ωcm and H = 25, 45 and 65 μm respectively, and showed insignificant variations in L_n; this behaviour is also observed in most comparisons of epilayers made on nearby slices of one series having the same resistivity.

More surprisingly, the value of L_n is influenced only little by the resistivity of the epilayer: for instance nearby slices 27 and 30 had epilayers of resistivity 2 Ωcm and 0.15 Ωcm respectively; the same is true for slices 36 and 40.

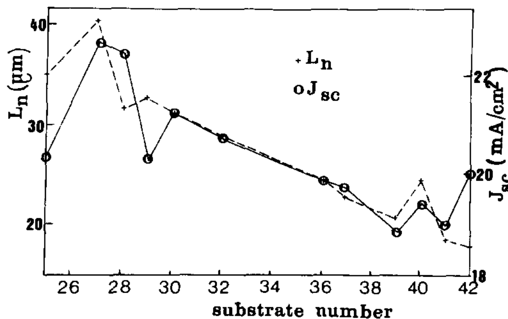

Fig. 6. Variation in short-circuit current J_{sc} (○) and epilayer electron diffusion length L_n (+) with substrate number along the B-doped ingot.

5. Discussion and conclusions

Let us discuss first the errors which may be related to the respective contributions to the quantum efficiency of the front layer, epilayer and substrate. The frontal dead layer produced by our screen-printing technology has a thickness of 0.4 - 0.5 μm, as determined from the rapid decrease in Q for wavelengths below 0.6 μm using the method described in ref. 25. Our choice of w which best fits the experiments (0.1 - 0.3 μm) lies between the thickness of the dead layer and that of the depleted region (which is near 0.1 μm), and this fit is only slightly sensitive to the chosen value of w. This shows that our approximation can account for both the absorption and the photogeneration in the front layer, and therefore that it introduces negligible error.

The error in the epilayer contribution to Q arises from uncertainties in the epilayer thickness H and back surface recombination velocity S_n. The influence of H is very large, but this parameter is rather well known. The calculation of S_n implied rough approximations, but we observed that our result for L_n was not very sensitive to the chosen value of S_n. This is not surprising: an analysis by Arora *et al.* [26] showed that S_n influences the overall efficiency very much but the short-circuit current J_{sc} only little (compare Figs. 8 and 7 of ref. 26: the variation in J_{sc} when S_n changes from 40 to 600 cm^2 s^{-1} is only 2%). Our method of course uses short-circuit currents.

We have neglected the photocurrent generated in a substrate of resistivity 0.03 Ωcm and diffusion length before cell processing of 19 μm. In order to estimate the error thus involved, we have applied the exact model [15] to cells 25, 28, 32 and 36. The best fits with this model are compared with those of our simple model in Table 2. For all cases involving thick (40 - 60 μm) epilayers, the exact model is not at all sensitive to the value of L_{ns}, so that the contribution of the substrate can be considered as negligible; we also discovered a tendency for S_n to be higher than the theoretical value used in the simple model, which together with the large epilayer thickness may

TABLE 2

Comparison of simple (this work) and exact ([15]) models

Cell no.	*Best fit of simple model*		*Possible fits using the exact model*		
	S_n (cm s^{-1})	L_n (μm)	L_{ns} (μm)	S_n (cm s^{-1})	L_n (μm)
WBRC 3536	45	24.8	0 - 20	1000 - 10 000	20 - 25
WBRC 3528	45	32.0	0 - 20	2000 - 20 000	32 - 36
WBRC 3532	600	29.4	0 - 20	1000 - 10 000	25 - 30
WBRC 3525	45	35.4	0 - 5	1000 - 5000	30 - 35
WBRC 3525	45	35.4	5 - 10	5000 - 10 000	30 - 35
WBRC 3525	45	35.4	0 - 5	0 - 1000	25 - 30
WBRC 3525	45	35.4	5 - 10	1000 - 5000	25 - 30

explain the zero substrate contribution. For the thinnest epilayer encountered (sample 3525), a non-zero substrate contribution cannot be excluded; the three parameters then available (L_{ns}, S_n and L_n) allow several different fits to be obtained, but the best ones use L_{ns} values smaller than 5 μm and S_n values of the order of 1000 cm s^{-1}. The experimental value of Q in the 0.85 - 1.0 μm wavelength range is incompatible with any choice implying $L_{ns} > 10$ μm (too large a Q) or $S_n > 10\,000$ cm s^{-1} (too small a Q); L_n values in the range 25 - 35 μm together with S_n values between 1000 and 5000 cm s^{-1} are the only ones able to account successfully for the value of Q in the 0.7 - 0.85 μm range. In conclusion, we must accept that the substrate diffusion length has been damaged during cell processing, so that substrate contribution is always small and in most cases negligible.

We conclude that the simple model may use slight underestimates for S_n and give slight overestimates for L_n, but it is able to define L_n values which are accurate to within 15% and can be used to make valid comparisons between different solar cells made on the same substrate.

We can now discuss how the values of L_n depend on the physical characteristics of the epilayers. At first glance, it is surprising to find almost the same values of L_n for epilayers of quite different boron doping levels (1×10^{16} and 1.3×10^{17} cm^{-3}): with single crystals, the material with the highest doping level should have a short-circuit current 10 - 15% less than that with the lowest doping level [27, 28]. However this is no longer true for polycrystals, where this effect is largely compensated by the fall in the potential barrier at grain boundaries due to high doping levels: according to ref. 28 the difference in J_{sc} is reduced to less than 5% if the grain size is less than 200 μm and the interface state density 5×10^{11} cm^{-2}. The corresponding variations in L_n with doping should be even less than those in J_{sc}. Evidently our epilayers have relatively low quality because of their low grain size and non-negligible nickel content, two defects originating from the substrates which were used. The almost regular decrease in L_n when the substrate number increases is probably related to the observed increase in intragranular defect density from the bottom to the top of the ingot.

Another rather accurate determination of L_n can be made by applying the LBIC method to the epilayer, without actually building a solar cell, under the condition that L_n is much smaller than the epilayer thickness H. Specially thick epilayers were grown on two substrates, and LBIC measurements were made on them using a GaAs laser, with the following results

Sample 31: $H = 62$ μm, $\rho = 0.15$ Ωcm: $L_n = 53$ μm

Sample 43: $H = 64$ μm, $\rho = 1.6$ Ωcm: $L_n = 40$ μm

Here again we note that the determining factor which controls L_n is the crystalline quality rather than the layer doping level. When complete solar cells were built on nearby substrates, the values of L_n determined from their spectral responses were near 30 μm and 20 μm respectively. The differences

between these two sets of values emphasize again the damage introduced by the screen printing process, which implies annealing of the epilayer/screen printing paste interfaces at temperatures which may reach 900 °C.

In conclusion, our interpretation of the spectral response of epitaxial solar cells makes it possible to determine the electron diffusion length in the epilayer, even if the latter is very thin, provided that the epilayer thickness is accurately known and that the substrate is highly doped.

For the low quality substrates used ($L_{ns} \simeq 10$ μm after cell processing), the epilayers have improved values of L_n (20 - 40 μm), which are well correlated with the short-circuit currents of the solar cells built on them.

Acknowledgments

We thank S. N. Singh for having sent us a preprint of ref. 15 and allowing us to use his model in order to estimate the contribution of the substrate to the photoresponse. We are grateful to J. M. Laroche and Le Hoang Thi To for their help in measurement and simulation work. This work was part of Contracts EN 350075 and EN 350074 placed by the European Communities under the Solar Energy Program.

References

1 A. M. Goodman, *J. Appl. Phys.*, *32* (1961) 2550.
2 A. M. Goodman, L. A. Goodman and H. F. Gossenberger, *RCA Rev.*, *44* (1983) 326.
3 E. W. Wang, C. R. Baraona and H. W. Brandhorst, *J. Electrochem. Soc.*, *121* (1974) 973.
4 *Annual Book of ASTM Standards*, ASTM, Philadelphia, PA, 1979, F. 391, Part 43 (Electronics) pp. 770 - 778.
5 E. D. Stokes and T. L. Chu, *Appl. Phys. Lett.*, *30* (1977) 425.
6 A. Agarwal, V. J. Tewari, S. K. Agarwal and S. C. Jain, *Solid State Electron.*, *23* (1980) 1021.
7 R. Schwartz and C. Matthey, *Helv. Phys. Acta*, *57* (1984) 687.
8 J. A. Rand and A. M. Barnett, *Proc. 18th IEEE Photovoltaic Specialists Conf., Las Vegas, NV, October 21 - 25, 1985*, IEEE, New York, 1985, p. 831.
9 W. E. Phillips, *Solid State Electron.*, *15* (1972) 1097.
10 J. E. Bourée, Le Quang N., M. Barbé, V. Perraki-Goutsou and M. Rodot, *Proc. 6th EC Photovoltaic Solar Energy Conf.*, Reidel, Dordrecht, 1985, p. 1051.
11 H. J. Hovel, *Semiconductors and Semimetals, Vol. 11*, Academic Press, New York, 1975, p. 19.
12 T. L. Chu and S. S. Chu, *Sol. Energy Mater.*, *2* (1979 - 80) 265.
13 M. Caymax, V. Perraki, J. L. Pastol, J. E. Bourée, M. Eyckmans, M. Mertens, G. Revel and M. Rodot, *Proc. 2nd Int. Photovoltaic Science and Engineering Conf., Beijing, 1986*, p. 171.
14 M. Rodot, M. Barbé, J. E. Bourée, V. Perraki, G. Revel, R. Kishore, J. L. Pastol, R. Mertens, M. Caymax and M. Eyckmans, *Rev. Phys. Appl.*, *22* (1987) 687.
15 S. N. Singh, *Proc. 3rd Int. Photovoltaic Science and Engineering Conf., Tokyo, 1987*, to be published.
16 P. de Pauw, Thesis, Leuven, 1984.
17 W. Schmidt, K. D. Rasch and K. Roy, *Proc. 6th EC Photovoltaic Solar Energy Conf.*, Reidel, Dordrecht, 1985, p. 906.

18 M. P. Godlewski, C. R. Baraona and H. W. Brandhorst, Jr., *Proc. 10th IEEE Photovoltaic Specialists Conf.*, IEEE, New York, 1973, p. 40.
19 J. del Alamo, J. Van Meerbergen, F. d'Hoore and J. Nijs, *Solid State Electron.*, *24* (1981) 533.
20 G. Revel, D. Hania and J. L. Pastol, *Poly-Micro-Crystalline and Amorphous Semiconductors*, Ed. de Physique, Paris, 1982, p. 147.
21 J. Dzewior and D. Silber, *Appl. Phys. Lett.*, *35* (1979) 170.
22 R. Mertens, G. Cheek, P. de Pauw and L. Frisson, *Proc. 5th EC Photovoltaic Solar Energy Conf.*, Reidel, Dordrecht, 1983, p. 976.
R. Mertens, P. de Pauw, M. Eyckmans, M. Caymax, J. Nijs, Q. Xiang and L. Frisson, *Proc. 6th EC Photovoltaic Solar Energy Conf.*, Reidel, Dordrecht, 1985, p. 935.
23 R. T. Swimm and K. A. Dumas, *J. Appl. Phys.*, *53* (1982) 7502.
24 H. C. Scheer and H. G. Wagemann, *Arch. Elektrotech.*, *66* (1983) 327.
25 S. N. Singh, N. K. Arora and N. P. Singh, *Sol. Cells*, *13* (1984 - 85) 271.
26 J. D. Arora, S. N. Singh and P. C. Mathur, *Solid State Electron.*, *24* (1981) 739.
27 P. M. Dunbar and J. R. Hauser, *Solid State Electron.*, *19* (1976) 95.
28 J. Dugas and J. Oualid, *Sol. Cells*, *20* (1987) 145.